Adnan Morshed[1]
Buddini Iroshika Karawdeniya[2]
Y.M. Nuwan D.Y. Bandara[2]
Min Jun Kim[2]
Prashanta Dutta[1]

[1]School of Mechanical and Materials Engineering, Washington State University, Pullman, WA, USA
[2]Department of Mechanical Engineering, Lyle School of Engineering, Southern Methodist University, Dallas, TX, USA

Received September 25, 2019
Revised December 5, 2019
Accepted December 8, 2019

Review

Mechanical characterization of vesicles and cells: A review

Vesicles perform many essential functions in all living organisms. They respond like a transducer to mechanical stress in converting the applied force into mechanical and biological responses. At the same time, both biochemical and biophysical signals influence the vesicular response in bearing mechanical loads. In recent years, liposomes, artificial lipid vesicles, have gained substantial attention from the pharmaceutical industry as a prospective drug carrier which can also serve as an artificial cell-mimetic system. The ability of these vesicles to enter through pores of even smaller size makes them ideal candidates for therapeutic agents to reach the infected sites effectively. Engineering of vesicles with desired mechanical properties that can encapsulate drugs and release as required is the prime challenge in this field. This requirement has led to the modifications of the composition of the bilayer membrane by adding cholesterol, sphingomyelin, etc. In this article, we review the manufacturing and characterization techniques of various artificial/synthetic vesicles. We particularly focus on the electric field-driven characterization techniques to determine different properties of vesicle and its membranes, such as bending rigidity, viscosity, capacitance, conductance, etc., which are indicators of their content and mobility. Similarities and differences between artificial vesicles, natural vesicles, and cells are highlighted throughout the manuscript since most of these artificial vesicles are intended for cell mimetic functions.

Keywords:
drug / electrodeformation / exosomes / rigidity / vesicles
DOI 10.1002/elps.201900362

1 Introduction

Vesicles are biological structures enclosed by a membrane made of one or more lipid bilayers. Although biological cells with a diameter of 10 to 30 μm perfectly fit the definition of a vesicle, traditionally the term has been used to describe intracellular and extracellular structures containing cytoplasmic fluids. These include smaller vesicles like endocytic transport vesicles [1], secretory synaptic vesicles [2], bacterial membrane vesicles [3], lysosomes [4], and exosomes [5] having a diameter ranging from 30 to 100 nm. However, larger vesicles are also common in plant, fungal, and animal cells like vacuoles and ectosomes, which can have diameter as large as 1 μm.

There is a vast array of vesicles at play on the cellular level. For instance, synaptic vesicles (Fig. 1A) communicate among neighboring neurons through transfer of neurotransmitters [6]. Larger microvesicles on the order of 200 nm (aka ectosomes) can bud directly from the membrane and are used by cells to transport exogenous antigens, enzymes, and other proteins [7]. Even viruses produce vesicles that also directly bud out of the infected cell and target healthy cells for further infection [8]. On the contrary, exosomes are represented by small vesicles of different sizes that are formed as the intraluminal vesicle by budding into early endosomes and multivesicular endosomes [9]. They are released from the cell through different mechanisms including exocytosis and membrane rupture (Fig. 1B). Different cells (in vitro and in vivo) release exosomes with dimensions between 30 and 150 nm generated by the endosomal system [10]. These extracellular vesicles are used for intercellular communication and membrane trafficking by carrying cell-specific proteins [11], lipids [12], or RNAs [13]. Exosomes might also be used as cell-free immunotherapeutic cancer vaccines [14–17]. Moreover, exosomes have been identified as biomarkers for diagnostic and prognostic purposes. For example, the stiffness of

Correspondence: Professor Prashanta Dutta, School of Mechanical and Materials Engineering, Washington State University, Pullman, WA 99164-2920, USA
E-mail: prashanta@wsu.edu

Abbreviations: **AFM**, atomic force microscopy; **DMPC**, 1,2-dimyristoyl-snglycero-3-phosphocholine; **DOPC**, 1,2-dioleoyl-sn-glycero-3-phosphocholine; **ED**, electrodynamic spectroscopy; **FL**, fluctuation spectroscopy; **GUV**, giant unilamellar vesicle; **MA**, micropipette aspiration; **MT**, magnetic tweezers; **POPC**, palmitoyl-oleoyl-phosphatidylcholine; **OT**, optical trapping/tweezers; **SM**, sphingomyelin; **SSN**, solid-state nanopores

Color online: See article online to view Figs. 1–3, 5, 6, 9, 11–16, 18, and 19 in color.

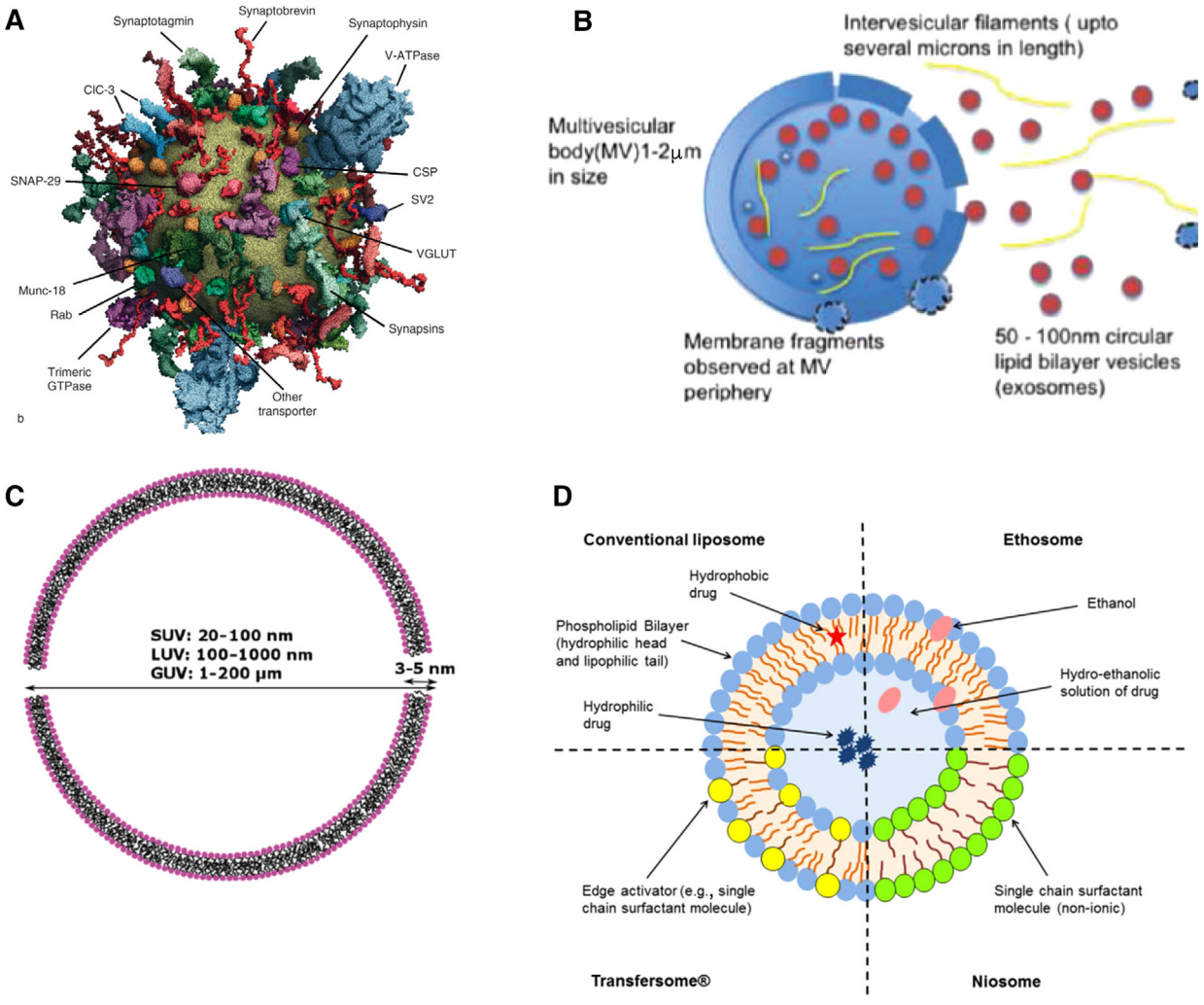

Figure 1. Different types of vesicles of interest. (A) Synaptic vesicles are one of the tiniest vesicles that are critical in neurophysiological communication. Reprinted from [6], Copyright (2009), with permission from Elsevier. (B) Human saliva-derived exosomes were recently identified to carry elevated levels of tumor-antigens for immunotherapeutic functions, thus acting as a biomarker for oral cancer. Reprinted with permission from [27]. Copyright (2011) American Chemical Society. (C) Unilamellar liposomal vesicles based on their size such as small (SUV), large (LUV), and giant (GUV) unilamellar vesicle. Both SUV and LUVs have been used in diagnostic and therapeutic applications [28], while GUVs have been used extensively in cell mimetic applications [29]. (D) Polymersomes with different surfactants added to the conventional liposomes for tuning the membrane property. Reprinted from [21].

exosomes originating from a tumor cell has recently been identified as a malignant-state dependent signature.

Like exosomes, human immune deficiency viruses (HIV) demonstrate remarkable changes in the mechanical properties with polymorphism. For instance, immature human immune deficiency viruses (HIV) is reported to be 14 times stiffer compared to its mature counterpart [18]. Hence, the study of mechanical deformability of virus can provide key insights for understanding the alterations in vesicle membrane structure with infectivity. These fascinating changes in mechanical behavior can be used for diagnosis of viral infection and progression of the disease.

A more recent drive in vesicle characterization research is coming from the need of micro- and nanoscale liposomal drug carriers with predictable mechanical characteristics. To this end, ultraflexible lipid vesicles have been designed to improve in-vitro skin delivery [19]. Mechanical characterization is crucial to understand, analyze, design, and evaluate the function of these biomimetic vesicles for optimum performance and to avoid any issues such as accidental overdosing. Characterization of these submicron and nanoscale vesicles is facilitated by the ever increasing repertoire of capabilities for measuring forces and displacements with picoNewton and nanometer resolutions, respectively [20].

Although vesicles can be varied in size and shape, the basic structure of most vesicle is very similar to liposomes. A liposome is a fluid-filled sack made of at least one lipid bilayer. Liposomes with a single lipid bilayer are often called unilamellar vesicles, while liposomes with multiple lipid bilayers are known as multilamellar vesicles. Conventional

unilamellar liposomes (Fig. 1C) are generally composed of phospholipids and cholesterol which encloses an aqueous core. Liposome characteristics can be modified by the addition of (i) surfactants to form transfersomes and niosomes (depending on the ratio of the phospholipid to surfactant), (ii) relatively high concentrations of ethanol to form ethosomes as shown in Fig. 1D [21]. Liposome-based artificial cells can serve as models to study cellular systems in a much simpler environment than the original cells. Liposomes, especially giant unilamellar vesicles (GUVs) provide a eukaryotic cell-like structure with similar membrane curvature for the study of membrane mechanical properties. These relatively large-sized vesicles can be observed by optical microscopes in microfluidic devices. However, as newer bacterial membrane vesicles [3] and exosomes [22] are coming to focus, study of these smaller vesicles are moving beyond the optical limit [23]. Atomic force microscopy (AFM) and other newer methods, such as optical and magnetic tweezers (MTs), have seen widespread use in characterizing this smaller breed of vesicles, although most of these techniques are low throughput [24]. Electrodeformation assays with optical visualization is another popular tool in large vesicle characterization [25], while electrodeformation techniques with solid-state nanopores (SSN) are now extending the limit of this useful nonintrusive method to nanosized vesicles [26].

In this review, we first give a brief overview of the different kinds of synthetic vesicle preparation methods. After that, we will briefly present the widely used characterization techniques in biological research such as AFM, optical tweezers (OT), MT, and micropipette aspiration (MA). In recent years, electric field-driven electrodeformation techniques have come into focus due to their nonintrusive and intrinsic high-throughput nature. The rest of this article will focus on the fundamental aspects of this electric field-driven characterization technique.

2 Vesicle formation techniques

The building block of vesicle membrane, phospholipids, are composed of hydrophilic head groups and hydrophobic tails that compel them to self-assemble to maintain stability in hydrophilic environments. In aqueous media, a planar bilayer of lipids tends to become spherical by enclosing some of the aqueous substance and forms a vesicle. These spherical vesicles are more commonly known as liposomes. Although most of the vesicles are unilamellar where the vesicle membrane consists of one lipid bilayer, it is possible to produce multilamellar vesicles or even vesicles with different lipid molecules at the two leaflets of the bilayer (aka asymmetric vesicles). Hybrid-biomimetic vesicles are designed by mimicking biological cells to overcome limitations of conventional vesicles. These vesicles are engineered for required properties such as size, shape, stability, ability to load therapeutic agents, and release them at specific targets [30, 31]. These vesicles are often prepared with surface ligands that target unhealthy tissue or disease site.

As mentioned earlier, traditional vesicle preparation techniques are based on swelling of a lipid layer into spheroidal sacks. Lipid film hydration is one of the most commonly used preparation methods for vesicles. The preparation of the vesicles starts with the lipids dissolved in an organic solvent (e.g., chloroform) and deposited on a solid substrate such as glass. The solvent is then evaporated under a nitrogen or argon stream followed by thorough evaporation under vacuum. The lipid layers are then hydrated with an aqueous buffer that causes lipid films to swell spontaneously due to the flow of the aqueous buffer solution between the lipid bilayer stacks as shown in Fig. 2A where a unilamellar vesicle forms from a single lipid bilayer [32]. When hydrating the stacks of bilayers, vesicles of varying lamellarity can be formed based on the hydration force used. The interlayer distance gets pronounced when there are thermal fluctuations or electrostatic repulsions between stacked bilayers, which enhances the flow of the buffer between layers. Therefore, use of some percentage of charged lipids facilitates efficient swelling. Furthermore, when using strong hydrodynamic flows, there is a higher possibility of multilamellar vesicle formation whereas slow flow rates will result in unilamellar vesicles [33]. Although procedurally very simple, it takes around 1–2 days to form vesicles in this process. Another flexible approach is to use a polymer-based gel as the substrate instead of a solid surface, and pump aqueous salt buffer solution through the porous polymer substrate for swelling and vesicle formation [33]. Force normal to the lipid bilayer prompts the liposome generation. Here, crowding of the vesicles results in the fusion of adjacent small liposomes making giant liposomes (Fig. 2B).

Electroforming is another swelling approach where a lipid thin film (dissolved in organic solvent) is deposited between two electrodes. Common electrodes include platinum [34], titanium [35], semiconductive glass plates coated with indium tin oxide (ITO) [36], stainless steel [37], and silicon substrates [38]. Once the organic solvent is evaporated, the aqueous buffer solution is added to hydrate the lipid bilayers. Next an electric field [34, 39, 40]—alternating current (AC) or direct current (DC)— is applied which strips off the lipid layer forcing it to self-assemble into monodispersed vesicles within a few hours (Fig. 2C). Another innovative way of swelling is pulsed jetting, where two aqueous droplets are placed in an organic solvent containing phospholipids. The lipid molecules gather around the aqueous-organic interface resulting in two aqueous droplets with a single layer of lipid molecules around them. Next, the two droplets are brought into contact which creates a planar lipid bilayer interface as shown in Fig. 2D. Finally, small volumes of aqueous substance are shot across the bilayer using a micronozzle. The bilayer envelops the jetted volumes and breaks off from the membrane to form individual vesicles [41].

Novel methods are also coming into the mainstream with the intention of forming artificial cell-mimetic vesicles for gene expression [42]. For example, the droplet emulsion transfer method relies on the construction of inner and outer lipid leaflets of the vesicle in two stages using an emulsion

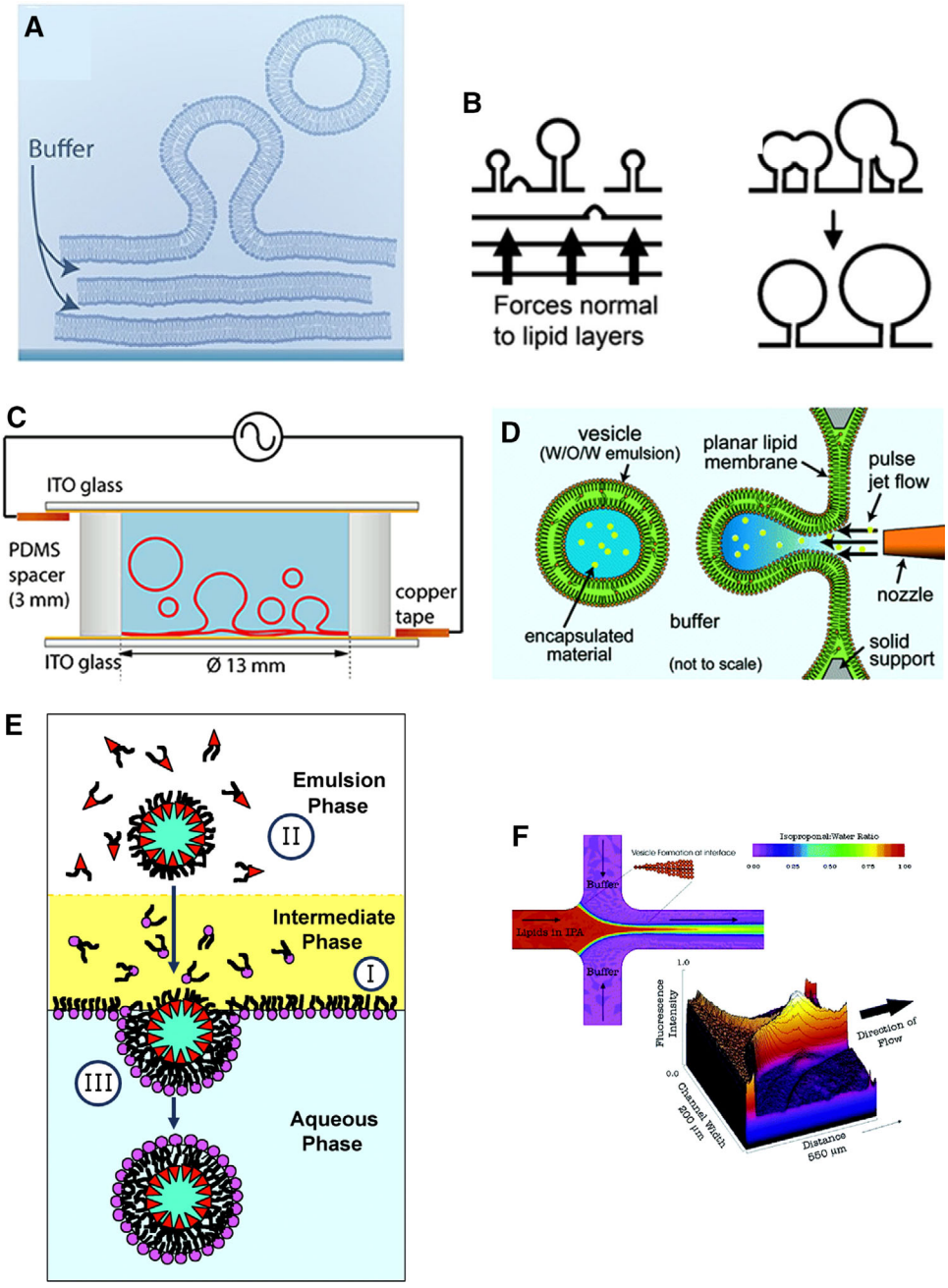

Figure 2. Common vesicle preparation methods. (A) Schematic showing unilamellar vesicle formation through lipid film hydration. Reprinted from [32]. (B) Gel assisted swelling. Reprinted with permission from [33], Copyright (2009) American Chemical Society. (C) Electroformation technique for vesicle preparation. Reprinted from [32]. (D) Schematic diagram of the pulsed jet method for vesicle formation. Reprinted with permission from [41], Copyright (2007) American Chemical Society. (E) Schematic representation of droplet emulsion transfer to make asymmetric vesicles [43]. Copyright (2003) National Academy of Sciences. (F) Schematic representation of the vesicle formation by flow focusing in a microfluidic channel where the concentration ratio of the alcohol is shown by the color contour. Reprinted from [44].

(top) and an aqueous (buffer) phase as shown in Fig. 2E. First, the intermediate phase between the emulsion and aqueous phase (middle layer in Fig. 2E) is preincubated with lipid molecules of the outer layer which saturates the interface and forms a monolayer. Next, the inner leaflet is formed in water-in-oil emulsion (top layer in Fig. 2E) by stabilizing water droplets via encapsulation of lipid molecules. Finally, the droplet made for the inner leaflet (from the top layer) is drawn through the interface under gravity or centrifugation force to the aqueous phase which forms an asymmetric (two different lipids in two leaflets) lipid bilayer vesicle as shown in Fig. 2E [43].

Lately, the advent of micro- and nanofluidic techniques has streamlined the vesicle preparation process in terms of space, time and cost. Jahn et al. [44] have shown an innovative way to form vesicles using microfluidic flow focusing in a cross-shaped microchannel. In their work, a lipid dissolved alcohol solution is injected to streams of aqueous buffers as shown in Fig. 2F. As the three flows travel together in the same channel, alcohol gets dissolve in water and the lipid molecules self-assemble into vesicles with a monodispersed distribution [44]. Another interesting approach is the transient membrane injection where amphiphilic lipid molecules get self-assembled into two separate monolayers at the two

Table 1. Overview of primary characteristics of different measurement techniques

	Optical tweezers	AFM	Micropipette aspiration	Magnetic tweezers	Electrodeformation
Spatial Resolution (nm)	0.1-2	0.5-1	25	5-10	10-10^6
Temporal resolution (s)	10^{-4}	10^{-3}	10^{-4}	10^{-1}-10^{-2}	10^{-4}
Stiffness (pN/nm)	0.005-1	10-10^5	N/A	10^{-3}-10^{-6}	N/A
Force range (pN)	0.1-100	10-10^4	0.3 (0.1-10 mbar)	10^{-3}-10^2	Variable
Displacement range (nm)	0.1-10^5	0.5-10^4	N/A	5-10^4	1-10^5
Probe size (μm)	0.25-5	100-250	N/A	0.5-5	N/A
Typical applications	Tethered assay; 3D manipulation	High force pulling and interaction assays	Vesicle mechanical properties measurement; single cell manipulation; tissue tension heterogeneity	Tethered assay; DNA topology	Vesicle electrical properties measurement; single cell manipulation
Advantages	Low-noise and low drift	High-resolution imaging	Economical	Specific interactions	Noninvasive; high throughput
Limitations	Photodamage; sample heating; nonspecific	Large high-stiffness probe; large minimal force; sample must be immobilized	Temporal resolution limited by visualization techniques	No manipulation (Force hysteresis)	Temporal resolution limited by visualization techniques; nonspecific

water-oil interfaces [45]. Detailed descriptions of each preparation process are out of scope for the present work, but interested readers are referred to review the article by Dimova [25].

3 Characterization processes

Study of the cellular mechanical properties dates back to several decades [46, 47]. However, the attention to the properties of exosomes and bioengineered vesicles are fairly recent. Vesicle manipulation techniques have been ever expanding with the traditional ones being miniaturized to single-molecule level [20]. The choice of the technique is largely determined by the type of vesicle and the exact property to be measured. Additionally, the spatial and temporal resolution along with the time required for reliable measurements become a deciding factor in choosing the experimental technique. Therefore, there is no single technique which is best for all measurements. And even for the measurement of a single property, variation is expected based on whether the property was measured locally on the vesicle membrane or the entire vesicle was deformed. We have summarized some key aspects in Table 1 for the five key characterization techniques reviewed in this manuscript.

3.1 Atomic force microscopy

AFM is popularly used for force spectroscopy where beam theory is used to determine the moduli of materials from the deflection of a cantilever tip [48]. Often a laser is used to measure the vertical displacement of a cantilever, and from these measurements, the force at the probing tip is calculated. A number of studies have been conducted on whole cells revealing properties like Young's modulus and the bending rigidity [49, 50]. More recently, several groups have studied the mechanical properties of liposomes with different chemical compositions [51]. Some of the key findings from these studies are summarized in Table 2.

The mathematical models used for property measurement from deformation data generally depend on the test conditions. Most prevalent models include shell and Hertz indentation model which consider the physical behavior of the cell (Fig. 3). In the Hertz model, the measured deflection (d) for a known applied force (F) at the probe tip can be connected to Young's modulus (E) as:

$$F = d^{3/2}\frac{2\pi}{3}\frac{E}{1-\upsilon^2}R_2{}^{1/2}, \tag{1}$$

where R_2 is the radius of curvature and υ is the Poisson's ratio of the membrane. Once Young's modulus is known, the bending rigidity (k_B) can be found using $k_B = Eh^3/12(1-\upsilon^2)$. In the case of large deformations, a combination of Hertzian and neo-Hookean formulations have been used to capture the force versus deformation profiles with very high accuracy [59]. Due to the relatively high stiffness of the cantilever probe, some of the biological samples are still very difficult to investigate using AFM. Moreover, the AFM technique is traditionally very low throughput.

Table 2. Comparison of mechanical properties of lipid membranes originating from different compositions of phospholipids

Lipid	Bending rigidity ($\times 10^{-19}$J)	Young's modulus (MPa)	Refs.
1,2-dioleoyl-sn-glycero-3-phosphocholine (DOPC)	0.88-8.65	27-150	[51–55]
1,2-dipalmitoyl-snglycero-3-phosphocholine (DPPC)	2.03-15.50	31-116	[51, 54]
1,2-dimyristoyl-snglycero-3-phosphocholine (DMPC)	1.15-1.27	24-26	[56, 57]
Egg sphingomyelin, cholesterol	12.94-27.72	140-300	[52, 53]
Mixture of unsaturated and saturated phosphatidylcholine (EggPC)	0.27	1.97	[58]

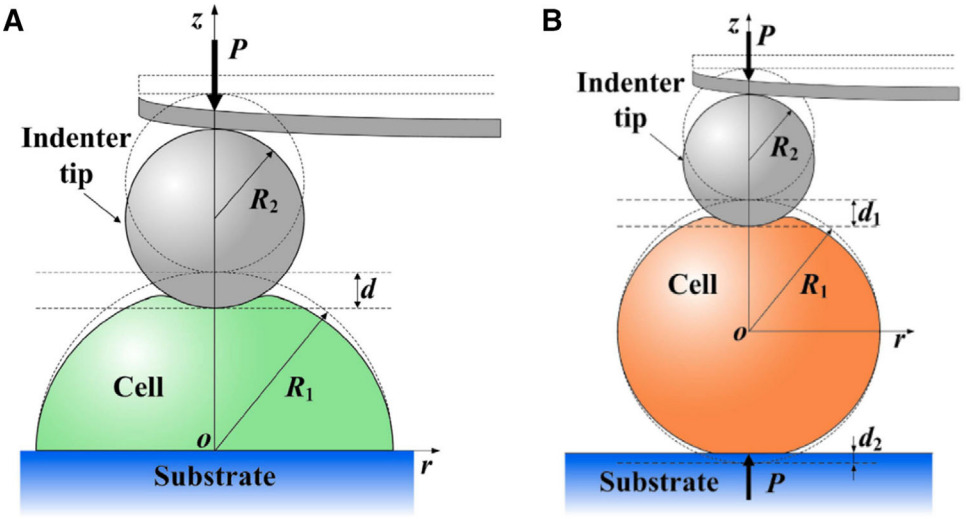

Figure 3. Schematic of indentation of a (A) hemispherical and (B) spherical cell. The cell with radius R_1 is located on a rigid flat substrate and indented by a spherical indenter of radius R_2. Reprinted from [59] with permission.

Although high-speed AFMs are starting to appear [60], samples needed to be immobilized in the majority of the experiments which is another major drawback of this technique. For sample immobilization, the surface must be very flat (roughness <0.5 nm). While immobilization of the sample on bare surfaces like muscovite mica is common, there are recent attempts to improve the stability of immobilization and initiate selective binding by functionalizing the surface with a charged polymer deposition [61,62] or an antibody coating [61, 63]. Though surface modification techniques would allow for better immobilization, it demands further expertise and preparations. Furthermore, the choice of the probe tip shape and media (e.g., aqueous, gel, etc.) are known to affect the measurements significantly [51].

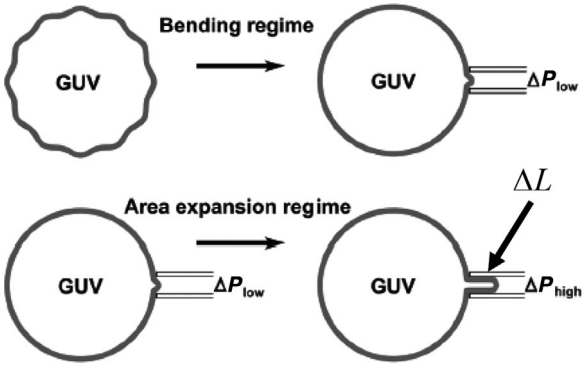

Figure 4. Schematic of tension–strain measurement of a giant unilamellar vesicle: (top) the bending regime and (bottom) area expansion regime. Reproduced from [64] with permission from the Royal Society of Chemistry, copyright 2016.

3.2 Micropipette aspiration

MA is one of the least expensive techniques to study the mechanics of whole-cell or vesicle membrane deformation. During the MA experiment, the membrane is pulled in (under vacuum) partially or completely into a glass tube of known inner diameter, where the micropipette diameter is generally much smaller than that of the vesicle. Upon a sustained suction, the membrane slips and deforms inside the tube. Studies have reported distinct bending and (membrane surface) area expansion regimes over extended periods of time [64]. In the bending regime (Fig. 4), the lipid bilayer behaves like an incompressible material conserving the total membrane area. On the other hand, in the area expansion regime with higher tensions, the membrane is strained due to the direct expansion of the surface area per lipid molecule [64].

The applied suction pressure can vary from 0.1 to 1 kPa, while the resolution of as low as ± 25 nm has been reported [65]. With a pressure differential ΔP, the applied force on the vesicle can be estimated as [66]:

$$F = \pi r_p^2 \Delta P \left(\frac{4r_v - r_p}{3r_p}\right)\left(1 - \frac{u_a}{u_f}\right), \quad (2)$$

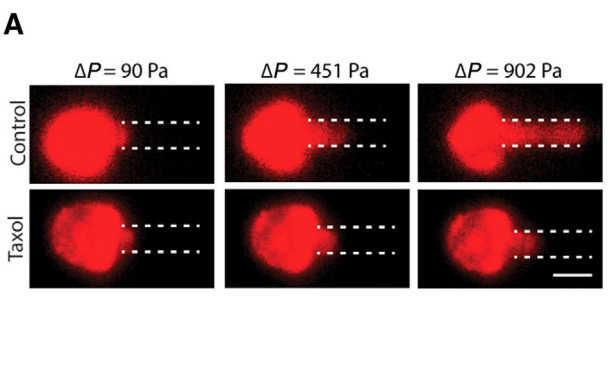

Figure 5. Change in breast cancer cell stiffness after exposure to Taxol. (A) Fluorescence image at different stages of aspiration (B) Young's modulus. Reprinted from [73] with permission of AIP Publishing.

where u_a and u_f are the velocities of the vesicle after and before suction under the pressure differential respectively; r_P and r_v are the radii of the micropipette and vesicle, respectively. The change in vesicle surface area (Δa) can be calculated using the lip (ΔL) formed inside the pipette as:

$$\Delta a = 2\pi R_P^2 \left(\frac{1}{r_P} - \frac{1}{r_v}\right) \Delta L. \tag{3}$$

From Δa, the area dilation modulus can be calculated using:

$$k_{area} = \frac{a_0}{\Delta a} \frac{\Delta P}{2} \left(\frac{1}{r_P} - \frac{1}{r_v}\right)^{-1}. \tag{4}$$

Experiments involving red blood cells [65, 67, 68], cytoskeletal actin [69, 70], and chondrocytes [71] have been conducted to measure the viscoelastic behavior and volume strains. More recently, GUVs with nanotubes embedded on the membrane surface was characterized using MA by Bhatia et al. [72]. Although those GUVs did not have any internal structure like cytoskeleton or organelles, they behaved like a cell membrane due to the increase in membrane stiffness owing to the embedded nanotubes on the surface. In general, MA can be used to track the change in cell membrane properties after modification by any foreign agents such as drugs. Lee et al. [73] have demonstrated the stiffening of breast cancer cells (MDA_MB-231) after introducing Taxol using MA in [73] as shown in Fig. 5.

Owing to the relatively simple hardware requirements, MA technique can easily be adapted to microfluidic setups compared to other techniques. However, it is much more difficult to apply picoNewton level forces achieved by AFM technique. Also, the physical size of the pipettes presents a lower limit of possible vesicle sizes that can be reliably aspirated. For further details on the recent developments in MA, readers are referred to [74].

3.3 Optical tweezers and trapping

Optical trapping (OT) is a highly versatile technique which can be applied on vesicles ranging from nanometers to micrometers. With submillisecond time resolution, this technique also allows the measurement of three-dimensional displacement. Unlike AFM or MA, OT does not require direct contact with the vesicle. In a typical optical trap, a highly focused laser beam is used to trap and manipulate microscopic, neutral objects such as small dielectric spherical particles and vesicles. When the particle diameter ($2r$) is small compared to the incident laser wavelength (λ_{inc}), it behaves like a point dipole in the optical field with distinct scattering and gradient forces. The scattering force rises from absorption and reradiation of light. The scattering force is proportional to the intensity of the light and acts in the direction of incident light propagation. For an incident intensity of I_0, the scattering force is given as [75]:

$$F_{scatt} = I_0 \left(\frac{m^2 - 1}{m^2 + 2}\right)^2 \frac{128 n_m \pi^5 r^6}{3c\lambda_{inc}^4}. \tag{5}$$

where n_m is the refractive index of the outside medium, m is the ratio of the refraction index of the particle/vesicle to the refractive index of the medium, and c is the speed of light. The gradient force, on the other hand, arises from the inhomogeneity in the optical field. The gradient force can be given as [75]:

$$F_{grad} = \frac{2\pi r^3}{c} \left(\frac{m^2 - 1}{m^2 + 2}\right) \nabla I_0. \tag{6}$$

The gradient force draws the particle into the region of the highest intensity, while the scattering force pulls the particle into an equilibrium position that is slightly downstream of the maximum intensity in the axial direction (Fig 6A). The balance between the two forces ends in stable trapping [76].

When the object diameter is large compared to the incident laser wavelength (λ_{inc}), some of the focused rays get reflected on the surface of the particle (rays R_1 and R_2 in Fig. 6B) imparting the scattering force. However, most of the incident rays get refracted successively through the object and emerges out. These emergent rays (A') transfer momentum backward following the conservation of momentum causing a substantial net backward trapping force (resultant of forces (F_A)in Fig. 6B) toward the higher light intensity. In equilibrium, this trapping force balances out the scattering force resulting in a stable trap [77].

Lipid vesicles and cells have been stably trapped using optical tweezers which can work on vesicles as small as 20 nm [78, 79]. OTs have also been incorporated into high throughout microfluidic devices for cell sorting and characterization

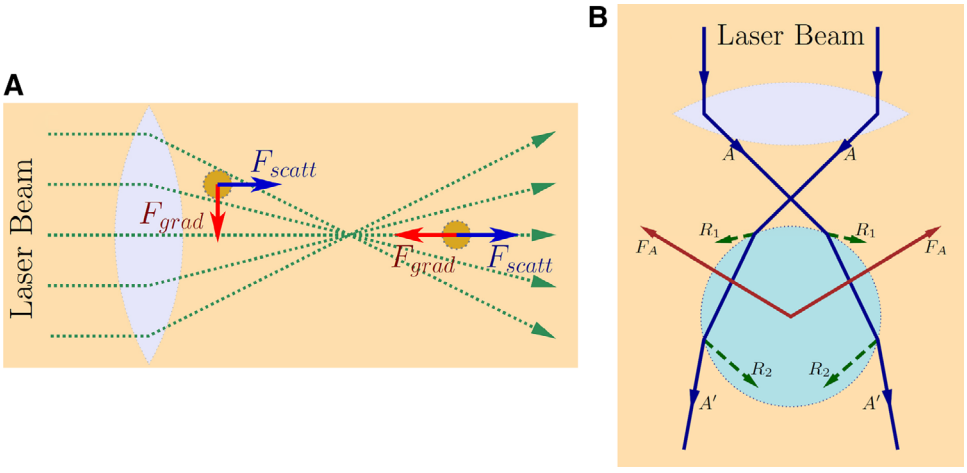

Figure 6. Vesicle trapping when the vesicle size is (A) smaller and (B) larger than the incident wavelength. (A) A particle is focused to a diffraction-limited beam waist created by a three-dimensional light gradient. (B) Backward forces (F_A) are arising due the emergent refracted rays A′ in larger objects.

Table 3. Comparison of mechanical properties of the cytoskeleton of different cells

Cell	Viscosity (Pa-s)	Cell rigidity scaling factor (Pa)
Fibroblast (NIH3T3)	0.15 ± 0.05	55 ± 5
Astrocytes	0.0 ± 0.06	36 ± 2
Neurons	0.09 ± 0.06	53 ± 4

Reproduced from [84] under the Creative Commons license.

[80]. Suresh et al. [81], used OT to characterize RBCs at different stages of growth, while Dao et al. [82] used optically trapped beads to deform cell membranes. Gross [83] trapped smaller lipid vesicles inside a eukaryotic cell. Ayala et. al. [84] reported viscoelastic moduli and viscosity of the cytoskeleton of different types of cells using a forced oscillatory displacement technique (Table 3). At low frequency, the Young's modulus (E) is on the same order of the cell rigidity scaling factor (G_0).

However, conventional OTs have an upper limit on the size of the vesicle that can be manipulated using a single trap. Although the picoNewton levels of force generated by OT are enough to study molecular bonds, whole-cell deformation is difficult in this approach. Yet, by using two focused lasers from opposite directions whole cells can be stretched out [85]. The unavoidable side effect of focused lasers on the vesicle is the localized heating [86, 87]. Overexposure can change the membrane and medium properties like density and viscosity and could even affect cell viability. To overcome these shortcomings, a number of studies focused on trapping beads which were tethered to the vesicle and used them for a direct contact deformation [75].

Additionally, OT also suffers from a lack of specificity. It is extremely difficult to be highly selective since any dielectric particle near the focus is drawn to the trap. To avoid trapping a large number of unwanted objects, extra care needs to be taken during sample preparation to minimize any freely diffusing objects. Moreover, the OTs are susceptible to optical perturbations and interferences. Also, the lower limit of the applied force is bound by the lowest stiffness necessary to trap a certain vesicle. Unless the focus point is dynamically adjustable, the range of space where measurements can be done becomes extremely limited.

3.4 Magnetic bead rheometry

Magnetic bead rheometry or MTs uses paramagnetic microbeads and localized magnetic fields. Microbeads are either attached to a cell or vesicle membrane and a localized magnetic field is used for manipulation of microbeads. By varying the magnetic field frequency and intensity, various membrane behaviors (e.g., creep) and its topology can be studied [88, 89]. Under an applied magnetic field $\bar{B}$, a bead of radius r, and relative permeability μ_b experiences a force (F) as [90]:

$$F = \frac{2\pi r^3}{\mu_0}\left(\frac{\mu_r - 1}{\mu_r + 2}\right)\nabla\left(B^2\right), \tag{7}$$

where μ_0 is the permeability of the free space. Although it is advantageous to use as small bead as possible, the applied force on the beads drops sharply with the size. Thus, most experiments use beads on the order of one micrometer. The beads are generally manufactured by embedding iron oxide domains in a polymer matrix [91]. For membrane attachment (Fig. 7), researchers have coated the beads with fibronectin and then attached them to integrin receptors on the cell surface [92].

Unlike OT, MT does not suffer from photodamage and heating. These two advantages led to its widespread use in DNA manipulation [93, 94], characterization of actin networks [95], the study of cell interior [96], and biomedicine [91]. Another interesting feature of the MT is the presence of a restoring torque due to the magnetic polarization anisotropy of the superparamagnetic beads. This feature opened up the possibility of using rotational enzymes [97] and rotational microrheology [98]. Additionally, since most materials have a

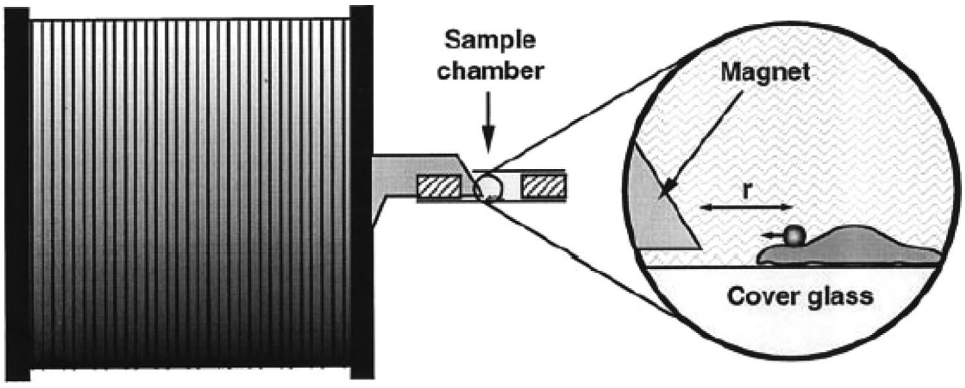

Figure 7. Magnetic bead rheometer set-up showing the paramagnetic bead attached to a soft body. Activation and deactivation of the electromagnet cause the bead movement. Reprinted from [92], Copyright (1998), with permission from the Biophysical Society.

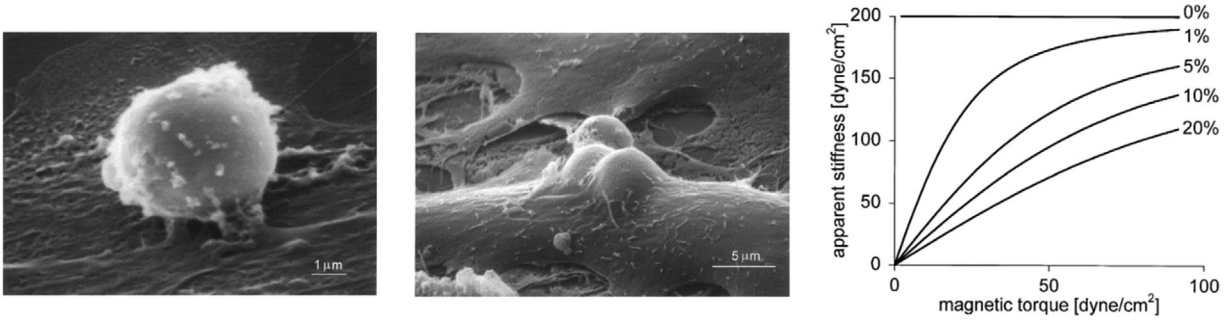

Figure 8. Magnetic twisting cytometry. Attachment (A) and internalization (B) of RGD peptide coated Fe_3O_4 beads on human airway smooth muscle cells. (C) Variation in stiffness measurements with different applied torque for various level of binding/internalization. Stiffness measurement is highly dependent on the level of binding which is difficult to control. Reprinted from [99], Copyright (1999), with permission from Elsevier.

low magnetic susceptibility, in general MT setups are free of interference compared to OT. However, due to complex and cumbersome control mechanisms, it is difficult to apply MT in high throughput applications. Also, unlike OT, the beads are not fixed in the three-dimensional space in MT since they produce a one-dimensional potential without a local minimum. For this reason, magnetic beads must be tethered to the membrane or DNA by some means. Also, existing visualization techniques limit direct measurements of small vesicles using MT. Magnetic twisting cytometry has been used to predict cell stiffness and viscosity by attaching ligand coated magnetic beads to cell membrane (Fig. 8A and B). However, bead inhomogeneity and fraction of unbounded beads result in large variability (Fig. 8C) in the measurements as reported in [99].

3.5 Electrodeformation

Biological vesicles exhibit a number of interesting responses when exposed to electric fields. The primary source of these responses is the contrast in electrical properties (e.g., conductivity (σ), permittivity (ε), etc.) between intra- and extravesicular media (Fig 9). For instance, in a DC electric field, if the fluid inside the vesicle is more polarizable than the outer one, the vesicle will be subjected to a stretching force due to the polarization [100]. In this case, the vesicle behaves like a conductor in the fluid media and it will be stretched in the direction of the electric field since it acquires a net positive charge near the negative (cathode) electrode and vice versa as shown in Fig. 9A. On the contrary, the vesicle will be initially compressed by the electric field when it is less polarizable due to the initial polarization where it acquires a net positive charge at the side close to the positive (anode) electrode and vice versa.

Early applications of electrodeformation on biovesicles were reported by Engelhardt et al. [101] on erythrocytes. Seifert carried out exhaustive experiments by varying the vesicle size and configuration [102]. With the widespread use of microfluidics, electrodeformation has become extremely popular with biological samples since it does not necessitate large infrastructures like AFM, OT, MT, or MA. Dimova et al. developed a number of novel experimental techniques for vesicle formation [103] and characterized large deformation and poration with both alternating (AC) and direct current (DC) fields [104–106] (Fig. 10). Cell mimetic behaviors, such as morphological changes and phase separation [107], as well as wrinkling and spheroidal deformation have been studied both theoretically and experimentally by Vlahovska et al. [105, 108, 109]. Zimmerman et al. [110] studied the relationship between applied potential and deformation while MacQueen et al. [111] calculated the elastic properties of cells using the Clausius–Mossotti factor with the effective dipole moment assumption.

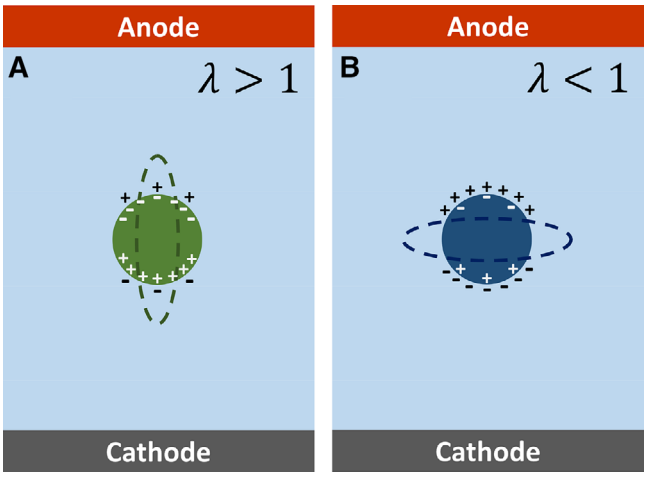

Figure 9. Vesicle initial polarization after application of an electric field causing electrodeformation from spherical to (A) prolate or (B) oblate spheroids. If the enclosed solution is more conducting than the suspending medium, $\lambda = (\sigma_{in}/\sigma_{out}) > 1$, the vesicle is pulled into a prolate ellipsoid. The polarization is reversed in the opposite case $\lambda < 1$and the vesicle deforms into an oblate ellipsoid.

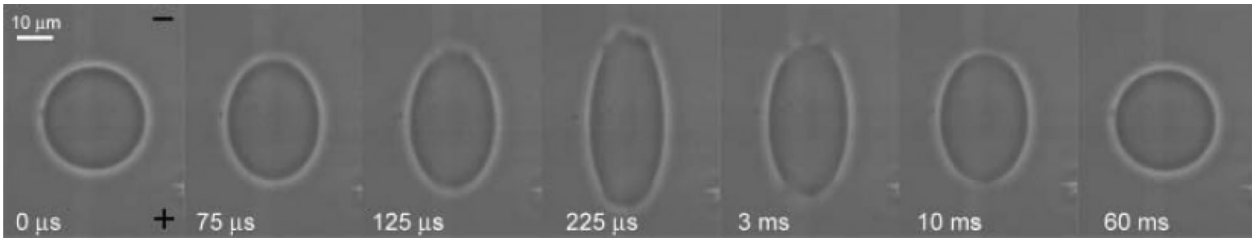

Figure 10. Image sequence (at 50 000 fps) of a vesicle under a nominal DC electric field, E = 2 kV/cm, and pulse duration of 200 μs. Macropores are observed first in the third frame at 125 μs. The electrode's polarity is indicated with a plus (+) and a minus (−) sign on the first snapshot. Reprinted from [105], Copyright (2005), with permission from the Biophysical Society.

In recent years, a lot of interest is being directed toward SSN for nanovesicle characterization [23] since optical detection technique used in traditional electrodeformation studies fail to detect nanosized vesicles. Nanopore technology has been widely used since its inception nearly two decades ago for DNA [112–114], proteins [115–117], glycans [118], viruses [26, 119], liposomes [23, 120], nanoparticles [121], and polymer[122] profiling because of its high resolution (single-molecule level), low-cost, high throughput, minimal sample requirement (both volume and concentration).

Figure 11A shows the schematic of a nanopore platform for characterization of vesicles or other biological samples. In brief, the nanopore separates two electrolyte reservoirs where the target vesicle is added to one side (*cis*) and a suitable voltage bias is applied to the other side (*trans*) to drive the vesicle from the *cis* side to the *trans* side across the nanopore either through electrophoresis or electro-osmosis (Fig. 11B). This transit phenomenon transiently blocks the open-pore ionic current and is restored once the vesicle escapes the nanopore—formally called an event. These events are characterized by the magnitude of the current drop (ΔI), duration of the current drop (Δt), and the frequency at which such blockages occur ($\Delta \nu$).

The relative current change ($\Delta I/I_0$) through a nanopore as a result of a particle transiting through it can be expressed as [123, 124]:

$$\frac{\Delta I}{I_0} = \frac{1}{G_0}\left(-\sigma_{out}\frac{\gamma\Lambda}{(L+1.6r_0)^2} + \mu_{mob}\frac{Q}{L^2}\right), \tag{8}$$

where I_0, G_0, σ_{out}, γ, Λ, L, r_0, μ_{mob}, and Q are the open pore (baseline) current, open-pore conductance, solution conductivity, shape factor, the excluded electrolyte volume of the particle, membrane length, pore radius, mobility of counter ions proximal to the nanopore surface, and the analyte surface charge respectively. For a generalized ellipsoid, the shape factor is related to the aspect ratio (α) as [125]:

$$\frac{1}{\gamma} = \frac{\alpha\cos^{-1}\alpha}{(1-\alpha^2)^{3/2}} - \frac{\alpha^2}{1-\alpha^2} \qquad \text{when } \alpha < 1, \tag{9}$$

and

$$\frac{1}{\gamma} = \frac{\alpha^2}{\alpha^2-1} - \frac{\alpha\cos^{-1}\alpha}{(\alpha^2-1)^{3/2}} \qquad \text{when } \alpha > 1. \tag{10}$$

Here a and b are the radius parallel and perpendicular to the electric field, respectively. Since soft nanoparticles undergo electrodeformation, the shape factor γ changes depending on its aspect ratio ($\alpha = a/b$) thus changing $\Delta I/I_0$.

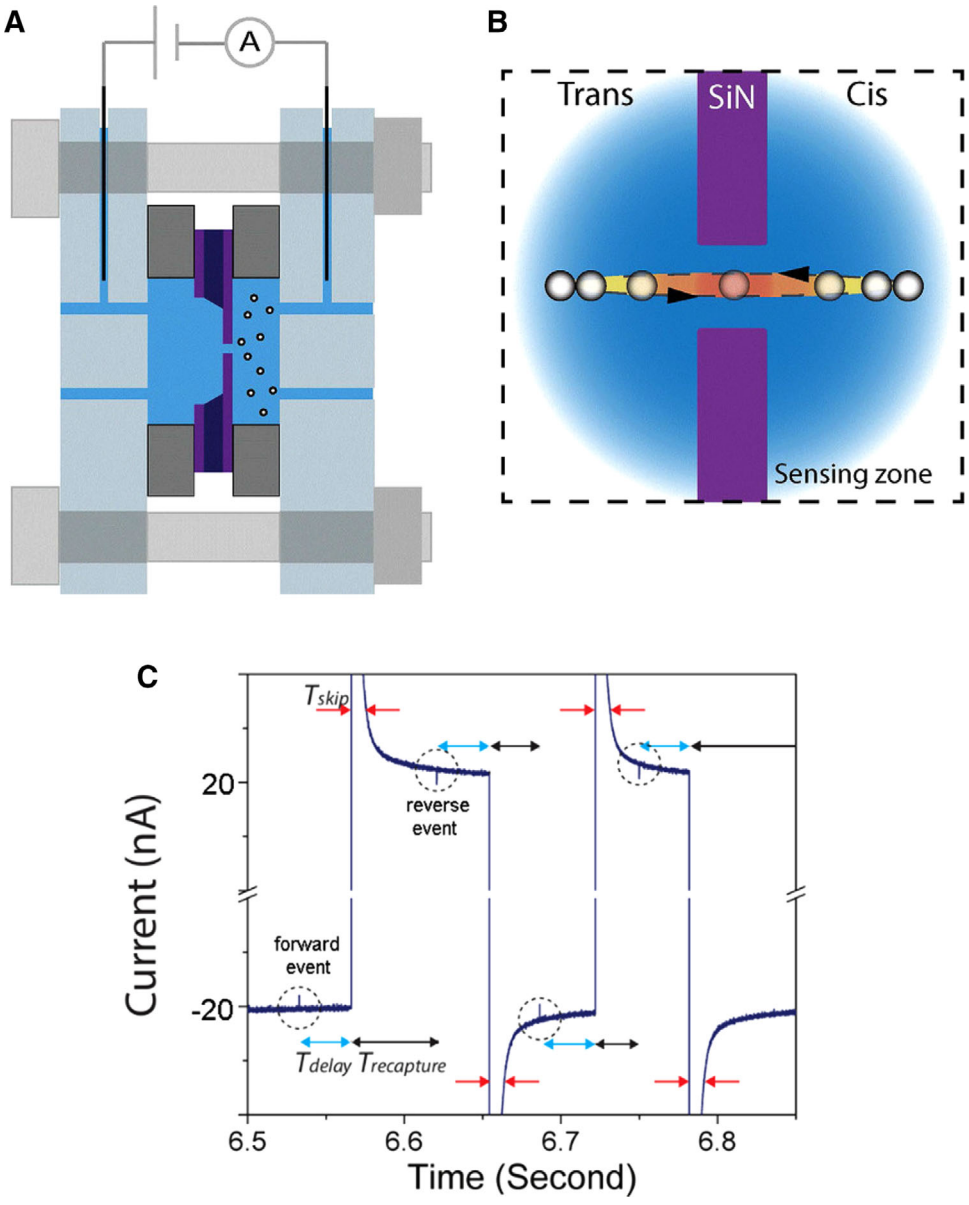

Figure 11. (A) A schematic figure of the flow cell and the nanopore chip, and (B) a schematic figure of the nanoparticle recapture event. Reprinted from [127] with permission. (C) Multiple recapture protocol with time domains T_{delay} (blue), $T_{recapture}$ (black), and T_{skip}(red) shown in arrows and events highlighted by black dotted circles. Reprinted from [120] with permission.

Hence, relative current change can be used as a metric to gauge the deformability of vesicle.

In vesicle characterization studies, SSN technique offers a number of advantages over its counterparts including size tunability, ability to withstand a wide range of physical and chemical conditions [124, 126]. Another major advantage of SSN technique is the minimal sample preparation requirement since vesicles can be added as-is which is a significant improvement over other methods such as AFM.

Recently, SSN assays were used to evaluate the electrodeformability of viruses and liposomes through a multiple recapture protocol [26, 120, 127]. The multiple recapture protocol would evaluate the membrane mechanical properties of single-vesicle multiple times (e.g., ∼25 times), thus, not only providing a statistically significant evaluation of the said properties of a single vesicle but also superseding conventional nanopore protocols which provide one value per translocating vesicle. The high throughput of nanopore platforms means that information from 1000's of vesicles can be gathered within a rapid time frame (typically tens of minutes).

The recapture protocol used to elucidate the relationship between the membrane rigidity is outlined in Fig. 11C. In brief, the applied voltage is reversed after a preset time (T_{delay}) from detecting an event. The data scanning is kept on-hold for a preset time (T_{skip}) to avoid the capacitive region before recording data for the recapturing event ($T_{recapture}$). This can be done multiple times (as many as ∼25 times). If no recapturing happens before ($T_{timeout}$) (a preset time unlike $T_{recapture}$), the recapture protocol will be aborted, and the voltage would return to its initial magnitude and sign.

In multiple recapture method, the electrodeformability is defined as the ratio of the relative current drop at forward to

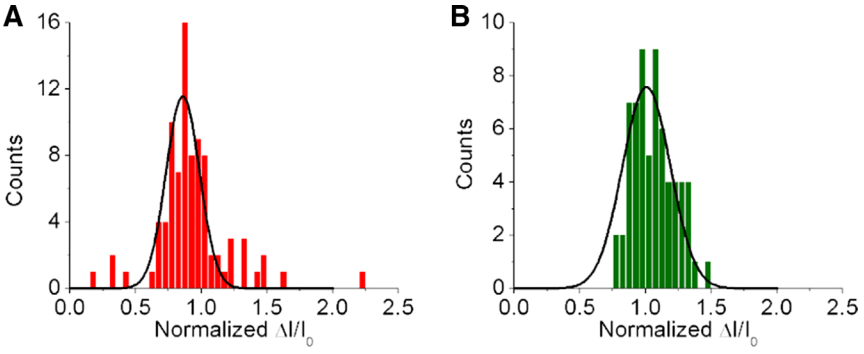

Figure 12. Recapture protocol using 100 mV (forward) and −100 mV (reverse) bias voltages with normalized $\Delta I/I_0\left(\left(\frac{\Delta I}{I_0}\right)_{\text{forward}}\Big/\left(\frac{\Delta I}{I_0}\right)_{\text{reverse}}\right)$ histograms of (**A**) liposome and (**B**) polystyrene. Reprinted from [120] with permission.

reverse voltage biases when the magnitude of reverse voltage is greater than or equal to the forward voltage;

$$\theta_{f,r} = \left(\frac{\Delta I}{I_0}\right)_{\text{forward}} \Big/ \left(\frac{\Delta I}{I_0}\right)_{\text{reverse}}. \tag{11}$$

When the particle deforms, $\theta_{f,r}$ would deviate from its ideally undeformed value of unity. However, it is imperative to first choose a voltage where the electrodeformation is minimal. Figure 12 presents the recapture events of liposomes (diameter of 115.9 ± 45.9 nm) and polystyrene beads (diameter of 104.5 ± 23.4 nm) with identical forward and reverse voltage magnitudes (±100 mV). Experimental results show that $\theta_{f,r}$ is centered around approximately 1 for both soft (liposome) and rigid (polystyrene) particles. A lower voltage could be attempted with the caveat of lower initial capture instance in addition to lower signal-to-noise ratio of a given event with respect to the baseline which could falsely trigger the recapture protocol through slight baseline shifts due to the lower onset thresholds warranted by lower ΔI of each event instance.

4 Governing equations for electrodeformation phenomena

4.1 Electric field

Electrohydrodynamic problems can usually be approximated as quasi-static phenomena [128]. The mathematical formulations for weakly conducting fluids separated by a membrane (leaky dielectric) began with Melcher and Taylor [129, 130]. In the absence of external magnetic fields, magnetic effects can be ignored completely in the leaky dielectric model. Using Maxwell's electromagnetic equations, the electric charge conservation can be expressed as [100, 131]:

$$\frac{\partial \rho_f}{\partial t} + \nabla \cdot \left(\rho_f \bar{v} + \bar{J}_D + \sigma \bar{E}\right) = 0, \tag{12}$$

where ε is the permittivity, ρ_f is the free charge density, $\bar{J}_D$ is the diffusive current, $\bar{v}$ is the fluid velocity vector, and σ is the conductivity, and $\bar{E}$ is the electric field vector. In most electrohydrodynamic systems, the diffusive current ($\bar{J}_D$) is much smaller than the Ohmic conduction current [132]. Also, for most electrohydrodynamic applications with vesicles, the external flow field is either negligible or in the creeping regime. This leads to a simplified charge conservation equation:

$$\frac{\partial \rho_f}{\partial t} + \nabla \cdot \left(\sigma \bar{E}\right) = 0. \tag{13}$$

The preceding Ohmic model also assumes instantaneous charge relaxation. The electrical forces due to the difference in electrical properties across the membrane and the electric field can be found by taking the gradient of the Maxwell stress tensor ($\bar{\bar{T}}_{elec}$) [133,134]. Using the Korteweg–Helmholtz force density description, the electric force density can be expressed as [135]:

$$\bar{f}_{elec} = \rho_f \bar{E} - \frac{1}{2}E^2\nabla\varepsilon + \nabla\left[\frac{1}{2}\rho\left(\frac{\partial \varepsilon}{\partial \rho}\right)_T E^2\right] = \nabla \cdot \bar{\bar{T}}_{el}, \tag{14}$$

where $\bar{\bar{I}}$ is the unit tensor and ρ is the mass density of the media. Defining the ratios of conductivity ($\lambda = \sigma_{in}/\sigma_{out}$), permittivity ($\Lambda = \varepsilon_{in}/\varepsilon_{out}$) inside and outside the vesicle membrane, a number of characteristic parameters can be identified. For instance, the timescale for electric phenomena (also known as the charge relaxation time) is the ratio of the permittivity and conductivity ($t_c = \varepsilon/\sigma$) [128]. For an initially undeformed vesicle of radius r, nominal field strength E_0, and nominal electric stress $\tau_c = \varepsilon E_0^2$, the electrohydrodynamic deformation timescale can be estimated as $t_{el} = \mu/\tau_c$, where μ is the fluid viscosity. The surface tension timescale ($t_s = \mu r/\beta$) influences the relaxation toward equilibrium spherical shape where β is the interfacial tension. Combining the different timescales yield several important nondimensional parameters which govern the electrohydrodynamic flows. These include the charge relaxation time ratio ($\lambda/\Lambda = t_{c,out}/t_{c,in}$), the capillary number ($Ca = t_s/t_{el}$) , and the electric Reynolds number ($\text{Re}_{el} = t_c/t_{el}$).

For the case of cells and vesicles where the lipid bilayer membrane acts as a leaky capacitor, the voltage jump across the membrane is given as V_{mem}. The capacitive charging of the membrane can be obtained from the continuity of current across the membrane as [136]:

$$C_{mem}\frac{dV_{mem}}{dt} + G_{mem}V_{mem} = \hat{n} \cdot \left(\sigma_{in}\bar{E}_{in}\right) = \hat{n} \cdot \left(\sigma_{out}\bar{E}_{out}\right). \tag{15}$$

Here, the membrane is modeled as a two-dimensional interface with effective capacitance $C_{mem} = \varepsilon_{mem}/h$ and

conductance $G_{mem} = \sigma_{mem}/h$, where h is the membrane thickness. The membrane characteristic time scale for charging is given as [137]:

$$t_{ch\,\mathrm{arg}\,e} = \frac{rC_{mem}}{\sigma_{in}}\left(1+\frac{\lambda}{2}\right). \tag{16}$$

For a typical lipid membrane, $t_{ch\,\mathrm{arg}\,e} \sim 1$ ms. In most EHD analysis, the displacement currents from the electrolytes are not considered, since both the Maxwell-Wagner time scale, $t_{MW} = (\varepsilon_{in} + 2\varepsilon_{out})/(\sigma_{in} + 2\sigma_{out})$ which governs the vesicle polarization time and the charge relaxation timescale (t_c) are small (~10 ns) when compared with the membrane-charging time ($t_{ch\,\mathrm{arg}\,e}$) and the electrohydrodynamic deformation time (t_{el}).

4.2 Deformation and membrane model

The lipid membrane of a cell/vesicle contains cholesterols, proteins, and channels. These membrane components change the stiffness of the membrane and restrict the movement of the phospholipid molecules of the membrane. Additionally, interactions between the cytoskeleton of the cell and these membrane components further restrict the flow of the membrane. This controls the extent of deformation that the cell can undergo. Cells, however, at different stages of their differentiation, expel unwanted membrane proteins by releasing small vesicles in the form of exosomes [138]. These exosomes share striking structural similarities with bioengineered liposomes. They do not contain cholesterols, proteins, channels, or a cytoskeleton. So, when a local strain is induced in the membrane of a liposome or exosome, the molecules of the membrane quickly reorganize themselves to reduce this strain, and the membrane rupture is avoided [139]. While in case of an actual cell, a similar strain might cause membrane breakdown or formation of pores on the membrane. This phenomenon highlights the need for distinction in mathematical representation when considering different kinds of vesicles. It is well understood that unlike most materials, the mechanical response of biomembranes cannot be simply characterized in terms of fixed properties [140]. Although originated from the shell theory, the mathematical formulation of biological membranes resulted in a number of constitutive relations due to the complex response of the vesicles.

One of the major approaches in modeling the vesicle membrane deformation is to treat it as a deformable two-dimensional surface with hyperelastic or viscoelastic properties [141]. This approach has been popular largely due to its primary roots going back to the theory of shells and due to the negligible thickness of the vesicle membranes. A constitutive law for a two-dimensional membrane can be obtained by extrapolating from a three-dimensional elastic relation to a thin material [142]. For example, the behavior of a membrane, consisting of an isotropic volume-incompressible material, may be described by the two-dimensional equivalent of the Mooney–Rivlin law which gives the in-plane surface tension as:

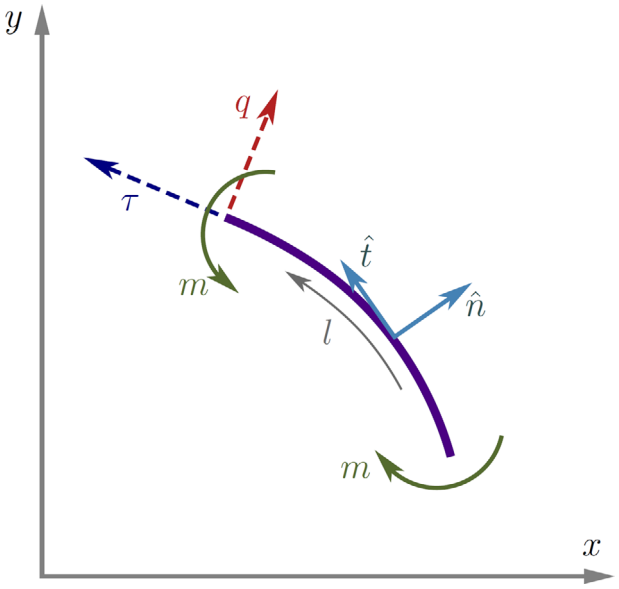

Figure 13. Side view of a 2D membrane showing the in-plane tension (τ) and the transverse tension (q) which creates the bending moment (m).

$$T_1^{MR} = \frac{G_{MR}}{\zeta_1\zeta_2}\left(\zeta_1^2 - \frac{1}{(\zeta_1\zeta_2)^2}\right)\left[\Psi + \zeta_2^2\,(1-\Psi)\right], \tag{17}$$

where G_{MR} (N/m) is an elastic modulus, ζ represents a principal extension ratio, and Ψ is a scalar coefficient between 0 and 1 with 1 corresponding to the neo-Hookean case. The subscripts 1 and 2 refer to the two local principal axes. Another approach is to directly postulate a two-dimensional constitutive law following experimental observations of the deformation characteristics. This approach was used, for example, by Skalak et al., and Evans for red blood cell membranes [46, 143].

Traditionally, the thinness assumption led to several orders of magnitude smaller tension components transverse to the surface (q) as shown in Fig. 13. However, the same is not true for polymerized membranes and biomembranes with anisotropy or a thicker shell. In a two-dimensional framework, the transverse shear tension (q) is related to the bending moment (m) through $q = dm/dl$, where l is the arc length. This leads to a modified tension:

$$\bar{T} = \tau\hat{t} + q\hat{n}, \tag{18}$$

where τ is the in-plane tension and $\hat{t}$ and $\hat{n}$ are the tangential and normal unit vectors, respectively.

Another common approach in mechanical membrane modeling is to consider a surface patch initially undeformed with uniform curvature, H, (e.g., planar sheets or perfect spheres) which are also isotropic. In this approach, the effect of the bending moment can be captured with a linear constitutive equation [144]. Canham [145] and Helfrich [146] proposed strain energy functions for this kind of linear

constitutive equation in the form of bending energy functionals as:

$$E = \frac{\kappa}{2}\int (2H_m - H_0)^2 dA + \kappa_G \int \Pi dA, \tag{19}$$

where the integration is over the instantaneous configuration of the membrane, H_m is the mean curvature of the two principal curvatures (H_1 and H_2), H_0 is the intrinsic curvature, $\Pi = H_1 H_2$ is the Gaussian curvature, and κ_G is bending modulus associated with the Gaussian curvature. It should be noted that Helfrich introduced the intrinsic curvature in the equation to consider the effects of asymmetry in the bilayer structure [144], and $H_0 = 0$ for symmetric membranes. For a two-dimensional membrane, setting $H_m = H/2$, where H is the membrane in-plane curvature, the total strain energy can be simplified to $E = \frac{\kappa}{2}\oint (H - H_0)^2 dl$ and the bending energy density can be expressed as $W_s = \frac{\kappa}{2}(H - H_0)^2$. Thus, the local bending moment (m) for calculating the transverse shear (q) in Eq. (19) can be found from,

$$m = \frac{dW_s}{dH} = \kappa\,(H - H_0)\,. \tag{20}$$

4.3 Flow field

Vesicle membrane electrodeformation is initiated by the electrical forces arising from the electric field distribution. However, since the vesicle itself is immersed in a fluid medium, the electric stress along with the hydrodynamic stress ($\bar{\bar{T}}_m = \mu(\partial_i u_j + \partial_j u_i) - \delta_{ij} P$) needs to be used in defining the flow behavior for the coupled system where P is the pressure. For an incompressible fluid, the electrohydrodynamic system can be described by modified Navier–Stokes and continuity equations as [100]:

$$\rho\frac{D\bar{u}}{Dt} = -\nabla P + \mu\nabla^2\bar{u} + \nabla\cdot\bar{\bar{T}}_{el}, \tag{21}$$

$$\nabla\cdot\bar{u} = 0, \tag{22}$$

where the flow field must satisfy the interfacial stress ($\tau_{mem} = \hat{n}\cdot[(\bar{\bar{T}}_{m,out} - \bar{\bar{T}}_{m,in}) + (\bar{\bar{T}}_{el,out} - \bar{\bar{T}}_{el,in})]$) arising from the differences in hydrodynamic and electric forces due to the discontinuities in electrical and mechanical properties. Additional boundary conditions required for solving the governing equations include the continuity of electric current and velocity across the membrane. Further details on these constitutive laws are beyond the scope for the present review. Interested readers are directed to [147] and [144] for a broader discussion.

5 Vesicle deformation in applied electric field

The deformation modes of soft vesicles under electric forces depend on several factors such as the permittivity and conductivity of the different fluid media, membrane mechanical response, nature of the applied electric field, the electric charge distribution in the fluid media, imposed flow, etc. Models of this complex phenomena, therefore, need to account for the different underlying physics in order to capture proper membrane deformation behavior. Nevertheless, the polarizability of the fluid media inside and outside the vesicle plays the most critical role in vesicle electrodeformation. The transient response due to charge imbalance across the membrane leads to prolate (oblate) deformations when the vesicle contents are more (less) conductive than the surrounding [107, 131] (Fig. 14). In the ($\lambda < 1$)case, with DC fields, the vesicle eventually deforms back to a prolate shape due to the build-up of the transmembrane potential across the vesicle membrane which behaves like a capacitor (following Eq. [(15)]) [148]. Assuming the vesicle to be a perfect sphere at all times, the transmembrane potential can be expressed as [149]:

$$V_{mem} = \frac{3}{2} r E_0 \left(1 - \exp\left(\frac{-t}{t_{ch\,\arg e}}\right)\right)\cos\theta, \tag{23}$$

where θ is the angle between the electric field direction and the position at the interface. Obviously, soft vesicles deform under electrohydrodynamic forcing and do not remain a perfect sphere. Numerical solutions for transmembrane potential in Eq. (15) are therefore necessary for nonspherical vesicles [131].

In the case of an alternating current (AC) field, the scenario is further complicated with a dependence on the electric field frequency. The critical frequency for AC electric field can be found using

$$\nu_{crit} = \frac{\sigma_{mem}}{rC_{mem}}[(1-\lambda)(\lambda+3)]^{-3/2}, \tag{24}$$

For an applied electric field frequency lower than the critical frequency this oblate to prolate transition appears in the vesicles (Fig. 15) [150, 151]. When the time is greater than $t_{ch\,\arg e}$, for any λ in DC field (or for low frequencies in AC with $\nu < \nu_{crit}$), the membrane capacitor is fully charged and the membrane behaves like a perfect insulator. This results in the vesicle shape change to a prolate ellipsoid.

Quite a few theoretical and numerical solutions have been presented for the solution of electrohydrodynamic equations. Initial analytical work on vesicles by Hyuga et al. [152,153] was focused on small transient pulses using perturbation theory. Sadik et al. [154] later expanded the solutions to a more general case with varying inner and outer conductivity for various applied fields. Interestingly, their analytical framework did not consider the membrane capacitive charging explicitly. Considering an ellipsoid with axes a and b ($a > b$), they expressed the deformation of the vesicle in terms of a shape factor (Θ) using,

$$\alpha = \frac{a}{b} = \frac{1}{\cos\Theta}; \quad \xi_0 = \frac{a}{\sqrt{a^2 - b^2}} = \frac{1}{\sin\Theta}. \tag{25}$$

The curvature-elastic energy ($V = \frac{\kappa a\pi}{3b\sin\Theta}[14\cos\Theta\sin\Theta + 6\Theta + 4\cos^3\Theta\sin\Theta]$) is then used to obtain the equation of motion as:

$$2K_0\frac{d^2\Theta}{dt^2} + \frac{dK_0}{d\Theta}\left(\frac{d\Theta}{dt}\right)^2 + \frac{dV}{d\Theta} - Q_\mu\frac{d\Theta}{dt} - Q_F = 0, \tag{26}$$

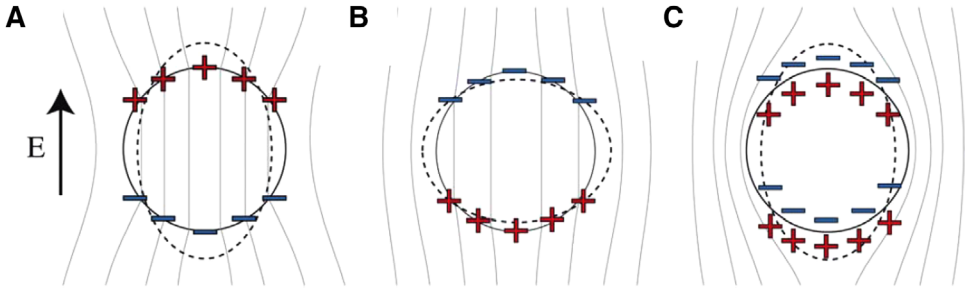

Figure 14. Schematic of the electric field lines and induced charge distribution around a vesicle immersed in an electrolyte solution following the imposition of a uniform DC field (A) time $< t_{charge}$ and $\lambda > 1$, (B) time $< t_{charge}$ and $\lambda < 1$, and (C) fully charged membrane capacitor (time $> t_{charge}$) and any λ. The dashed lines indicate the vesicle deformation. Reproduced from [107] with permission from the Royal Society of Chemistry.

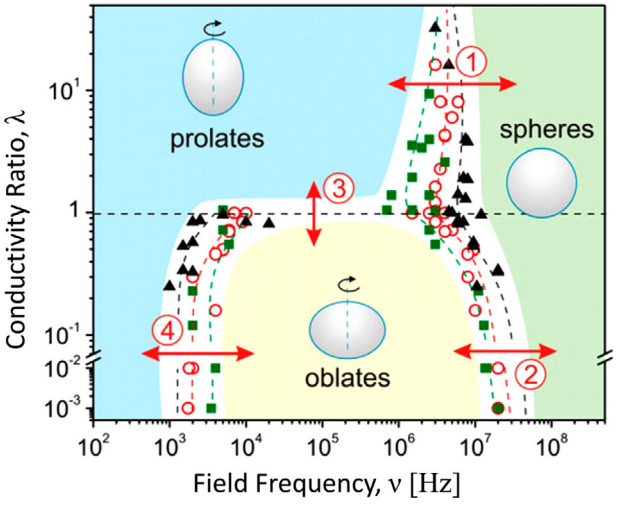

Figure 15. Phase representation of lipid vesicle shapes subjected to AC field frequency ν at different conductivity ratios λ. Reprinted from[151], Copyright (2008), with permission from the Biophysical Society.

where κ is the curvature elastic modulus. K_0, Q_μ, and Q_F are functions of the shape factor Θ, nominal electric field (E), pulse duration, and material properties like mass density, viscosity, and permittivity [154]. The solution of Eq. (25) leads to the instantaneous value of the shape factor from which the aspect ratio can be calculated using Eq. (24). Additionally, in a spherical co-ordinate system (ξ, η), the instantaneous normal component of velocity at a point on the deforming membrane can be found using,

$$u_n = \frac{b\sin\Theta\eta^2 + \frac{db}{d\Theta}\cos\Theta}{\cos\Theta\sqrt{1-\eta^2\sin^2\Theta}}\frac{d\Theta}{dt}, \tag{27}$$

which leads to the instantaneous position of the vesicle in the domain. It should be noted that their analytical model assumed a conserved vesicle surface area, which does not allow the area dilation they observed in their experiments. Although their analytical solution predicts the functional relationship between the extent of deformation and vesicle size, the model results failed to predict the experimental data on aspect ratio. Interestingly, a numerical solution by Morshed et al. found results (between vesicle size and aspect ratio) comparable to experiments, when membrane charging was considered [131] (Fig. 16).

Several other numerical works also presented vesicle deformation results using immersed interface and level set scheme [155] and boundary integral technique [156]. Zhang et al. presented a similarity solution for vesicle deformation and relaxation [157]. Instead of a constant surface area assumption like Sadik et al. [154], they considered the vesicle volume to be conserved. Additionally, the capacitive charging of the membranes was incorporated in their solution. According to their analytical model, the increase in apparent membrane area due to the electric forces and fluid-structure interactions is [157]:

$$\Delta a_s = \frac{k_B T}{8\pi\kappa}\ln\frac{\Gamma}{\Gamma_0} + \frac{\Gamma-\Gamma_0}{K_a}, \tag{28}$$

where Γ and Γ_0 are the membrane tension and initial membrane tension, respectively, k_B is the Boltzmann constant and κ is the bending rigidity, and K_a is the elastic stretching modulus. Here, the first term on the right side represents the thermal undulatory unfolding, and the second term represents elastic stretching. Figure 17A shows the apparent area changes from their model at different initial membrane tensions. When the areal extension is small, the membrane area increase is primarily due to the flattening of the shape fluctuations. In this regime, the area change exhibits an exponential correlation with membrane tension. However, at larger extension regimes, the area increase is attributed to the elastic stretching where the correlation is linear. It must be noted that unlike droplet deformation where surface tension is a property, for vesicle membrane deformation, the membrane tension appears as a constraint in the equations.

Schwalbe et al. [148] also presented an analytical solution starting from Helfrich curvature energy formulation for the membrane. A dimensionless parameter (Mason number, $Mn = \frac{\varepsilon_{out}E_0^2}{\mu_{out}\dot{\gamma}}$) involving electric and viscous stresses is used to identify different regimes of deformation under imposed flow at various viscosity ratios (Fig. 17B).

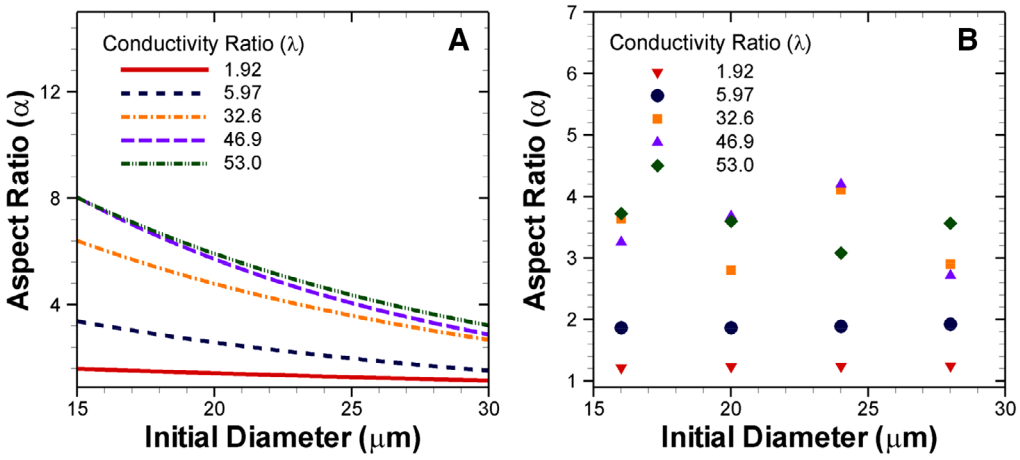

Figure 16. Predicted vesicle aspect ratio at 500 μs when an initially spherical vesicle is subjected to a nominal electric field of 1.5 kV/cm. (A) No voltage jump across the membrane and (B) voltage jump originating from membrane charging. For voltage jump across the membrane, there is no underlying relation between vesicle size and the extent of deformation which is similar to the experimental observation of Sadik et al. [154]. Reprinted figures with permission from [131], Copyright (2018) by the American Physical Society.

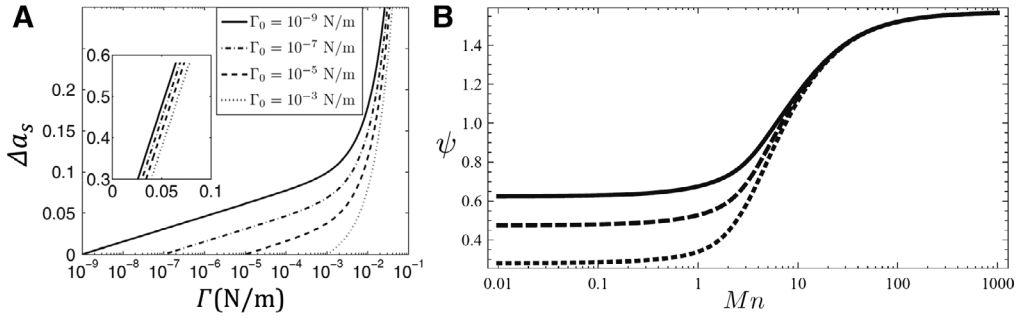

Figure 17. (A) The relative increase of the apparent area, Δa_s, as a function of membrane tension, Γ, for different values of initial membrane tension, Γ_0. Reprinted from [157] with permission of AIP Publishing. (B) Inclination angle (ψ) of vesicle at various Mn. The solid, dashed, and dotted curves are with viscosity ratio, μ_{in}/μ_{out} = 1, 3, and 5, respectively. Reprinted figure with permission from [148], Copyright (2011) by the American Physical Society.

6 Membrane properties from electrodeformation

Electrodeformation techniques are inherently advantageous in microfluidic and high-throughput applications. Several studies in the last ten years have started to apply different electrodeformation procedures for vesicle characterization in micro- and nanofluidic platforms. Generally, electrodeformation can be used for the determination of electrical properties of vesicles. Additionally, a number of flow and mechanical deformation associated properties have also been characterized using different electrodeformation techniques. In the following section, we highlight several electrodeformation based methods to characterize a number of different properties of vesicles.

6.1 Bending rigidity

Yu et al. used the vesicle relaxation dynamics during DC pulses to determine the tension and bending rigidity of vesicles for different concentrations of cholesterol [158]. In their work, the vesicle is first deformed to an ellipsoidal shape from its initial spherical form and then the electric field is turned off. In the absence of an electric field, the vesicle relaxes back to a spherical shape. They identified an initial entropic regime where the vesicles reverse their shape much quickly. These restoring dynamics differ depending on the concentrations of cholesterol present in the palmitoyl-oleoyl-phosphatidylcholine (POPC) membrane (Fig. 18A). Higher concentrations of cholesterol led to steeper descent indicating an increase in bending rigidity.

During postpulse vesicle relaxation, for moderate values of initial tension, Γ_0, and small to moderate deformations, the elastic deformation (second) term in Eq. (28) can be ignored, and the simplified equation can be rearranged to:

$$\frac{\Gamma}{\Gamma_0} = \exp\left(\frac{8\pi\kappa\Delta a_s}{k_B T}\right). \tag{29}$$

In this simplified model, the instantaneous membrane tension (Γ) was evaluated to be on the order of 10^{-6} N/m (Supplementary Material of [158]). Once the change in the

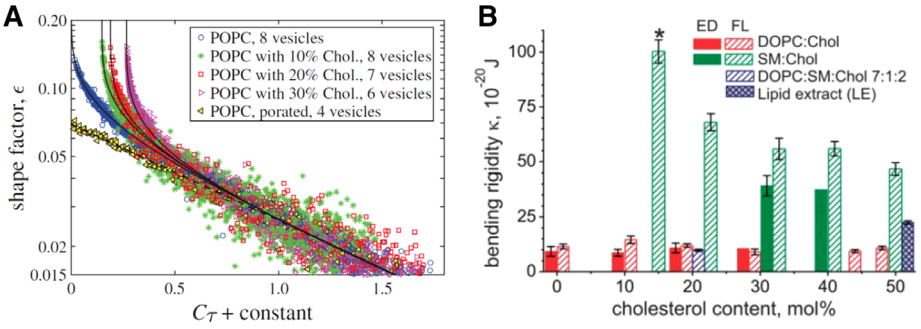

Figure 18. (A) Theoretical predictions (solid and dashed lines), and experimental results of relaxation of POPC vesicles with various cholesterol mole fractions. The shape factor is defined as $\epsilon = \alpha - 1$. Here $\tau = \frac{time \times \Gamma_0}{r \mu_{out}}$, and $C = \frac{24}{(32+23\mu_{in}/\mu_{out})}$. Reprinted figure with permission from [158], Copyright (2015) by the American Physical Society. (B) Bending rigidity of DOPC membranes made of different lipids as measured by (i) the electrodeformation method (ED: solid bars) and (ii) fluctuation spectroscopy (FL: hatched bars). Reproduced from [159] with permission from the Royal Society of Chemistry.

area (Δa_s) is evaluated experimentally, the bending rigidity could be derived using the above equation for different values of membrane tension. The initial membrane tension (Γ_0) is assessed from the extrapolation of experimental data shown in Fig. 18A.

Gracia et al. [159] used electric stresses to evaluate the membrane tension on the deformed vesicle. This tension is then utilized to calculate the variation in bending rigidity with a change in cholesterol content of the membrane. Differences in their measured results using electrodynamic (ED) and fluctuation spectroscopy (FL) highlight the underestimation in electrodeformation method for stiffer vesicles (SM:Chol). However, for softer vesicles (e.g., 1,2-dioleoyl-sn-glycero-3-phosphocholine [DOPC]:Chol) the measurements in both techniques are in good agreement as shown in Fig. 18B. Their experimental observation shows that depending on the base lipid molecule, the bending rigidity changes markedly with increasing cholesterol content. Unlike POPC in [158], DOPC does not exhibit any direct effect of cholesterol content on bending rigidity. Egg sphingomyelin (SM) on the contrary shows a reverse trend where the bending rigidity decreases with increasing cholesterol.

6.2 Edge tension and viscosity

The membrane viscosity affects the vesicle relaxation under DC pulses. Salipante et al. [107] incorporated the membrane viscosity in the governing equations (see [107] for details). The resulting solution (shape evolution with time data) was fitted to estimate the membrane viscosity (Fig. 19). Their results indicate that membrane viscosity slows the rate of deformation, but does not change the equilibrium shape and has no influence on the maximum deformation.

Portet et al. [160] used the resealing dynamics of an electroporated vesicle to measure the membrane edge tension. They presented the time-dependent radius of a circular pore (r_p) on an electroporated vesicle of initial radius r as a function of membrane tension (Γ), vesicle size and surrounding media dynamic viscosity (μ) as:

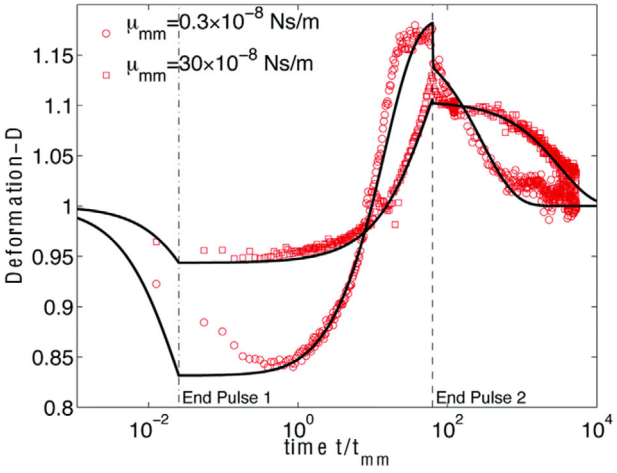

Figure 19. Deformation of a vesicle with an initial DC pulse of strength 400 kV/m for 20 ms, and a subsequent pulse of 20 kV/m for 50 ms. Reproduced from [107] with permission from the Royal Society of Chemistry.

$$r^2 \ln r_p = -\frac{2\Gamma}{3\pi\mu} t + C, \tag{30}$$

where C is a time dependent constant (One C value for each experiment). The slope of the linear portion of time versus $(r^2 \ln r_p)$ curve yields the edge tension as $\Gamma = -(3/2)\pi\mu \times$ slope, as shown in Fig. 20.

6.3 Capacitance and conductivity

In an AC electric field, the vesicle deformation switches from prolate to oblate at the critical frequency presented in Eq. (23). Salipante et al. used frequency-dependent vesicle shape change to calculate the capacitance [161]. Their

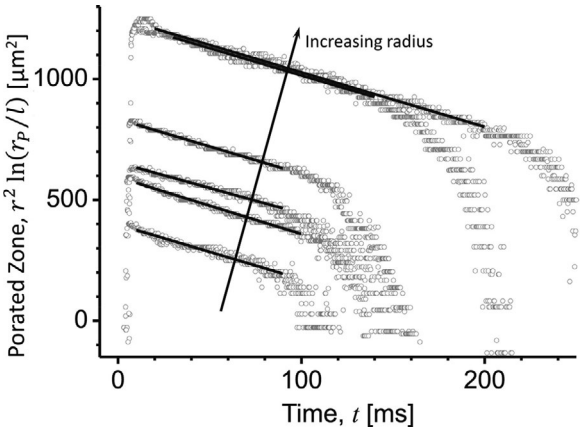

Figure 20. Evolution of the porated region as characterized by six different mixture of unsaturated and saturated phosphatidylcholine (EggPC) vesicles. The experimental data are represented by the gray open circles and the solid lines are linear fits. The vesicle radii, *r*, are (lower to upper) 12.7, 16.0, 17.6, 21.1, 20.7, and 21.7 μm. Reprinted from [160], Copyright (2010), with permission from the Biophysical Society.

experimental observations showed at low frequencies (sub-kHz), the vesicle shape always evolves to a prolate ellipsoid regardless of the solution conductivities and size of the vesicle. However, for higher frequencies (above MHz), the vesicle retains its spherical shape. At intermediate frequencies, a vesicle filled with a less conducting solution, $\lambda < 1$, deforms into an oblate ellipsoid.

Figure 21A shows that the critical frequency increases linearly with the inverse of the vesicle radius, which is inline with the model Eq. (24). Also, from the experimentally determined critical frequency, one can find the membrane capacitance (C_{mem}) for the known value of vesicle equilibrium radius. They also explored the effect of salt concentration of the membrane-enclosed solution on the membrane capacitance. From their experimental data, the capacitance of the bare membrane (C_B) can be found from:

$$\frac{1}{C_{mem}} = \frac{1}{C_{D,in}} + \frac{1}{C_B} + \frac{1}{C_{D,out}}, \tag{31}$$

where $C_{D,in}$ and $C_{D,out}$ are the capacitance of ionic solution inside and outside of the vesicle. Under a linear capacitor assumption, the double-layer capacitance can be found from the capacitance of a planar capacitor with a thickness of Debye length (κ_D)and the dielectric constant of the solution [137]. When the ionic strength of the solution is increased, it decreases the Debye length. Hence, the combined capacitance of the electrolyte–membrane system increases with increasing ionic concentration to an upper limit given by the bilayer capacitance (C_B)as shown in Fig. 21B.

Similar to capacitance, conductivity plays a major role in membrane deformation behavior. In micro- and nanofluidic setups, it is often convenient to translocate vesicles through pores of known dimensions and allow them to deform due to the electric and fluid field-driven forces. Morshed et al. used solid-state nanopore-based vesicle translocation data to track the change in local current and overall conductivity as vesicles translocate through the pore [162].

7 Future directions

In biomedical research, new applications are being introduced constantly using cell-derived vesicles as well as artificial vesicles. Study of their behaviors broadened the understanding of a number of complex phenomena including lipid assembly and viscoelasticity, polymerization, interactions with proteins and peptides, poration and fusion, etc. To keep up with the demand for various drug/biologic delivery, newer synthesis techniques are introduced. For instance, highly efficient exosome extraction processes from in-vivo dendritic cells have been designed [16]. Unilamellar vesicles being an excellent cell-mimetic system have led to preparation of miniature vesicles that closely resemble different organelles. Biomimetic nanovesicles with different inner and outer layers and varying surface protein to lipid ratios are being developed actively [30].

As the vesicles are evolving due to the change in the membrane composition or cargo content, proper characterization techniques must be in place for evaluation of their mechanical and electrical characteristics. In particular, the development of high throughput characterization techniques is needed for their widespread use in biological and clinical applications. Although traditional characterization techniques are inherently low throughput, each of these techniques are being implemented in microfluidic variants for parallel and continuous operation. For instance, Favre et al. have developed a two-dimensional AFM probe array (5 × 7) with 100 μm cantilevers for parallel position sensing using a CMOS camera [163]. Optical stretchers applied directly on vesicles have increased the characterization speed significantly [85]. Electrodeformation assays are being miniaturized and automated for faster applications.

Several key areas are identified that demands particular focus going forward.

1. Since most of the techniques measure specific characteristics, the focus should be shifted toward combining a number of characterization assays on the same device which can also provide time-dependent deformation results.
2. Combination of numerical and experimental approach has been fruitful in predicting vesicle behavior inside SSN. But this kind of synergistic approach is yet to be expanded to its full potential. As vesicles are moving toward submicron and nanoscales, co-ordination between theoretical, numerical, and experimental approaches are necessary to understand physics exclusive to this length and time scale more than ever.
3. As the nanovesicle research moves beyond the optical limit, it is essential that both theoretical and numerical works be extended to the nanometer length scales where electrical charge crowding and colloidal physics need particular attention.

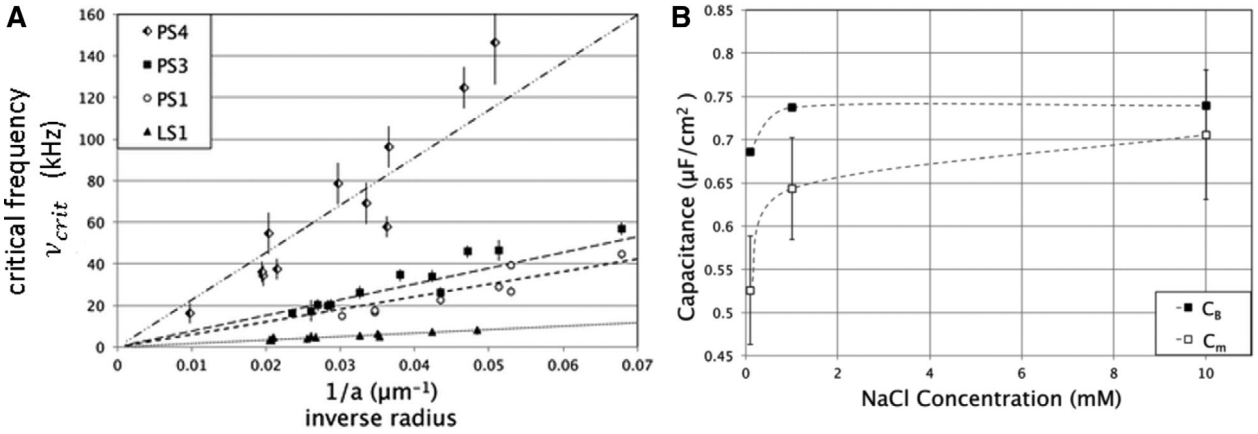

Figure 21. (A) Critical frequency, ν_{crit}, for the oblate–prolate transition as a function of the inverse radius of vesicles made of POPC (LS1) and polymersomes made of PS1, PS3, and PS4 for conductivity ratio, $\lambda = 0.25$. (B) Total specific membrane capacitance at different interior solution conductivities (salt concentrations) for POPC vesicles. The bilayer capacitance is obtained by subtracting the contribution of the double layers according to Eq. (30). The exterior conductivity was varied to produce a conductivity ratio within 0.1–0.3. Reproduced from [161] with permission from the Royal Society of Chemistry.

4. Finally, membrane mechanical descriptions for mesoscale models also need careful consideration when choosing between different types of vesicles. This is particularly crucial in the study of novel vesicles, such as polymersomes and viruses, whose membrane deformation behavior vary noticeably from that of RBC or lipid-based endothelial cells.

This work was supported in part by the National Institute of General Medical Sciences of the National Institutes of Health under Award Number R01GM122081 and in part by the National Institute of Health (R03EB022759) and National Science Foundation (CMMI #1712069).

The authors have declared no conflict of interest.

8 References

[1] Progida, C., Bakke, O., *J. Cell Sci.* 2016, *129*, 3971–3982.

[2] Bennett, M. K., Scheller, R. H., *Annu. Rev. Biochem.* 1994, *63*, 63–100.

[3] Toyofuku, M., Nomura, N., Eberl, L., *Nat. Rev. Microbiol.* 2019, *17*, 13–24.

[4] Lawrence, R. E., Zoncu, R., *Nat. Cell Biol.* 2019, *21*, 133–142.

[5] Pegtel, D. M., Gould, S. J., *Annu. Rev. Biochem.* 2019, *88*, 487–514.

[6] Takamori, S., in: Squire, L. R. (Ed.), *Encyclopedia of Neuroscience*, Academic Press, Oxford 2009, pp. 801–808.

[7] Cocucci, E., Meldolesi, J., *Trends Cell Biol.* 2015, *25*, 364–372.

[8] Aiken, C., *Nature* 2015, *526*, 202–203.

[9] Shurtleff, M. J., Temoche-Diaz, M. M., Schekman, R., *Annu. Rev. Cancer Biol.* 2018, *2*, 395–411.

[10] McGough, I. J., Vincent, J. P., *Development* 2016, *143*, 2482–2493.

[11] Keller, S., Ridinger, J., Rupp, A.-K., Janssen, J. W., Altevogt, P., *J. Transl. Med.* 2011, *9*, 86.

[12] Colombo, M., Raposo, G., Théry, C., *Annu. Rev. Cell Dev. Biol.* 2014, *30*, 255–289.

[13] Valadi, H., Ekström, K., Bossios, A., Sjöstrand, M., Lee, J. J., Lötvall, J. O., *Nat. Cell Biol.* 2007, *9*, 654–659.

[14] Zitvogel, L., Regnault, A., Lozier, A., Wolfers, J., Flament, C., Tenza, D., Ricciardi-Castagnoli, P., Raposo, G., Amigorena, S., *Nat. Med.* 1998, *4*, 594–600.

[15] Delcayre, A., Shu, H., Le Pecq, J.-B., *Expert Rev. Anticancer Ther.* 2005, *5*, 537–547.

[16] Alvarez-Erviti, L., Seow, Y., Yin, H., Betts, C., Lakhal, S., Wood, M. J., *Nat. Biotechnol.* 2011, *29*, 341–345.

[17] Morse, M. A., Garst, J., Osada, T., Khan, S., Hobeika, A., Clay, T. M., Valente, N., Shreeniwas, R., Sutton, M. A., Delcayre, A., *J. Transl. Med.* 2005, *3*, 9.

[18] Kol, N., Shi, Y., Tsvitov, M., Barlam, D., Shneck, R. Z., Kay, M. S., Rousso, I., *Biophys. J.* 2007, *92*, 1777–1783.

[19] Elsayed, M. M. A., Abdallah, O. Y., Naggar, V. F., Khalafallah, N. M., *Int. J. Pharma.* 2007, *332*, 1–16.

[20] Bao, G., Suresh, S., *Nat. Mater.* 2003, *2*, 715–725.

[21] Hua, S., *Front. Pharmacol.* 2015, *6*, 1–5.

[22] van Niel, G., D'Angelo, G., Raposo, G., *Nat. Rev. Mol. Cell Biol.* 2018, *19*, 213–228.

[23] Goyal, G., Darvish, A., Kim, M. J., *Analyst* 2015, *140*, 4865–4873.

[24] Darling, E. M., Di Carlo, D., *Annu. Rev. Biomed. Eng.* 2015, *17*, 35–62.

[25] Dimova, R., *Annu. Rev. Biophys.* 2019, *48*, 93–119.

[26] Darvish, A., Lee, J. S., Peng, B., Saharia, J., VenkatKalyana Sundaram, R., Goyal, G., Bandara, N., Ahn, C. W., Kim, J., Dutta, P., Chaiken, I., Kim, M. J., *Electrophoresis* 2019, *40*, 776–783.

[27] Sharma, S., Gillespie, B. M., Palanisamy, V., Gimzewski, J. K., *Langmuir* 2011, *27*, 14394–14400.

[28] Akbarzadeh, A., Rezaei-Sadabady, R., Davaran, S., Joo, S. W., Zarghami, N., Hanifehpour, Y., Samiei, M., Kouhi, M., Nejati-Koshki, K., *Nanoscale Res. Lett.* 2013, *8*, 1–9.

[29] Rideau, E., Dimova, R., Schwille, P., Wurm, F. R., Landfester, K., *Chem. Soc. Rev.* 2018, *47*, 8572–8610.

[30] Molinaro, R., Evangelopoulos, M., Hoffman, J. R., Corbo, C., Taraballi, F., Martinez, J. O., Hartman, K. A., Cosco, D., Costa, G., Romeo, I., *Adv. Mater.* 2018, *30*, 1702749.

[31] Kotla, N. G., Chandrasekar, B., Rooney, P., Sivaraman, G., Larrañaga, A., Krishna, K. V., Pandit, A., Rochev, Y., *ACS Biomater. Sci. Eng.* 2017, *3*, 1262–1272.

[32] Stein, H., Spindler, S., Bonakdar, N., Wang, C., Sandoghdar, V., *Front. Physiol.* 2017, *8*, 63.

[33] Horger, K. S., Estes, D. J., Capone, R., Mayer, M., *J. Am. Chem. Soc.* 2009, *131*, 1810–1819.

[34] Angelova, M. I., Soléau, S., Méléard, P., Faucon, F., Bothorel, P., *Trends in Colloid and Interface Science VI*, Springer, Berlin, Germany 1992, pp. 127–131.

[35] Ayuyan, A. G., Cohen, F. S., *Biophys. J.* 2006, *91*, 2172–2183.

[36] Meleard, P., Bagatolli, L. A., Pott, T., *Methods Enzymol.* 2009, *465*, 161–176.

[37] Pereno, V., Carugo, D., Bau, L., Sezgin, E., Bernardino de la Serna, J., Eggeling, C., Stride, E., *ACS Omega* 2017, *2*, 994–1002.

[38] Le Berre, M., Yamada, A., Reck, L., Chen, Y., Baigl, D., *Langmuir* 2008, *24*, 2643–2649.

[39] Angelova, M. I., Dimitrov, D. S., *Faraday Discuss. Chem. Soc.* 1986, *81*, 303–311.

[40] Politano, T. J., Froude, V. E., Jing, B., Zhu, Y., *Colloids Surf. B* 2010, *79*, 75–82.

[41] Funakoshi, K., Suzuki, H., Takeuchi, S., *J. Am. Chem. Soc.* 2007, *129*, 12608–12609.

[42] Noireaux, V., Bar-Ziv, R., Godefroy, J., Salman, H., Libchaber, A., *Phys. Biol.* 2005, *2*, P1–P8.

[43] Pautot, S., Frisken, B. J., Weitz, D., *Proc. Natl. Acad. Sci. USA* 2003, *100*, 10718–10721.

[44] Jahn, A., Vreeland, W. N., Gaitan, M., Locascio, L. E., *J. Am. Chem. Soc.* 2004, *126*, 2674–2675.

[45] Ota, S., Yoshizawa, S., Takeuchi, S., *Angew. Chem., Int. Ed.* 2009, *48*, 6533–6537.

[46] Skalak, R., Tozeren, A., Zarda, R. P., Chien, S., *Biophys. J.* 1973, *13*, 245–264.

[47] Harvey, E. N., Danielli, J. F., *Biol. Rev.* 1938, *13*, 319–341.

[48] Binnig, G., Quate, C. F., Gerber, C., *Phys. Rev. Lett.* 1986, *56*, 930–933.

[49] Jaasma, M. J., Jackson, W. M., Keaveny, T. M., *Ann. Biomed. Eng.* 2006, *34*, 748–758.

[50] Gonzalez-Cruz, R. D., Fonseca, V. C., Darling, E. M., *Proc. Natl. Acad. Sci. USA* 2012, *109*, E1523–E1529.

[51] Et-Thakafy, O., Delorme, N., Gaillard, C., Mériadec, C., Artzner, F., Lopez, C., Guyomarc'h, F., *Langmuir* 2017, *33*, 5117–5126.

[52] Sullan, R. M. A., Li, J. K., Zou, S., *Langmuir* 2009, *25*, 7471–7477.

[53] Li, J. K., Sullan, R. M. A., Zou, S., *Langmuir* 2011, *27*, 1308–1313.

[54] Picas, L., Rico, F., Scheuring, S., *Biophys. J.* 2012, *102*, L1–L3.

[55] Hantz, E., Cao, A., Escaig, J., Taillandier, E., *Biochim. Biophys. Acta Biomembr.* 1986, *862*, 379–386.

[56] Meleard, P., Gerbeaud, C., Pott, T., FernandezPuente, L., Bivas, I., Mitov, M. D., Dufourcq, J., Bothorel, P., *Biophys. J.* 1997, *72*, 2616–2629.

[57] Duwe, H. P., Sackmann, E., *Phys. A* 1990, *163*, 410–428.

[58] Liang, X. M., Mao, G. Z., Ng, K. Y. S., *J. Colloid Interface Sci.* 2004, *278*, 53–62.

[59] Ding, Y., Xu, G. K., Wang, G. F., *Sci. Rep.* 2017, *7*, 1–8.

[60] Ando, T., Kodera, N., Takai, E., Maruyama, D., Saito, K., Toda, A., *Proc. Natl. Acad. Sci. USA* 2001, *98*, 12468–12472.

[61] Sebaihi, N., De Boeck, B., Yuana, Y., Nieuwland, R., Pétry, J., *Meas. Sci. Technol.* 2017, *28*, 034006.

[62] Woo, J., Sharma, S., Gimzewski, J., *J. Circ. Biomarkers* 2016, *5*, 1–9.

[63] Hardij, J., Cecchet, F., Berquand, A., Gheldof, D., Chatelain, C., Mullier, F., Chatelain, B., Dogné, J.-M., *J. Extracell. Vesicles* 2013, *2*, 1–9.

[64] Lu, L., Doak, W. J., Schertzer, J. W., Chiarot, P. R., *Soft Matter* 2016, *12*, 7521–7528.

[65] Hochmuth, R. M., *J. Biomech.* 2000, *33*, 15–22.

[66] Shao, J.-Y., *Adv. Biomech.* 2001, 47–51.

[67] Hochmuth, R. M., Tingbeall, H. P., Beaty, B. B., Needham, D., Transontay, R., *Biophys. J.* 1993, *64*, 1596–1601.

[68] Sato, M., Levesque, M. J., Nerem, R. M., *Arteriosclerosis* 1987, *7*, 276–286.

[69] Yeung, A., Evans, E., *Biophys. J.* 1989, *56*, 139–149.

[70] Evans, E., Yeung, A., *Biophys. J.* 1989, *56*, 151–160.

[71] Jones, W. R., Ting-Beall, H. P., Lee, G. M., Kelley, S. S., Hochmuth, R. M., Guilak, F., *J. Biomech.* 1999, *32*, 119–127.

[72] Bhatia, T., Agudo-Canalejo, J., Dimova, R., Lipowsky, R., *ACS Nano* 2018, *12*, 4478–4485.

[73] Lee, L. M., Lee, J. W., Chase, D., Gebrezgiabhier, D., Liu, A. P., *Biomicrofluidics* 2016, *10*, 054105.

[74] Gonzalez-Bermudez, B., Guinea, G. V., Plaza, G. R., *Biophys. J.* 2019, *116*, 587–594.

[75] Neuman, K. C., Block, S. M., *Rev. Sci. Instrum.* 2004, *75*, 2787–2809.

[76] Zhang, H., Liu, K. K., *J. R. Soc. Interface* 2008, *5*, 671–690.

[77] Ashkin, A., Dziedzic, J. M., Bjorkholm, J. E., Chu, S., *Optics Lett.* 1986, *11*, 288–290.

[78] Neuman, K. C., Chadd, E. H., Liou, G. F., Bergman, K., Block, S. M., *Biophys. J.* 1999, *77*, 2856–2863.

[79] Cherney, D. P., Bridges, T. E., Harris, J. M., *Anal. Chem.* 2004, *76*, 4920–4928.

[80] Enger, J., Goksor, M., Ramser, K., Hagberg, P., Hanstorp, D., *Lab Chip* 2004, *4*, 196–200.

[81] Suresh, S., Spatz, J., Mills, J. P., Micoulet, A., Dao, M., Lim, C. T., Beil, M., Seufferlein, T., *Acta Biomater*. 2005, *1*, 15–30.

[82] Dao, M., Lim, C. T., Suresh, S., *J. Mech. Phys. Solids* 2005, *53*, 493–494.

[83] Gross, S. P., *Methods in Enzymology*, Academic Press, Cambridge, MA 2003, pp. 162–174.

[84] Ayala, Y. A., Pontes, B., Ether, D. S., Pires, L. B., Araujo, G. R., Frases, S., Romao, L. F., Farina, M., Moura-Neto, V., Viana, N. B., Nussenzveig, H. M., *BMC Biophys*. 2016, *9*.

[85] Guck, J., Ananthakrishnan, R., Mahmood, H., Moon, T. J., Cunningham, C. C., Kas, J., *Biophys. J.* 2001, *81*, 767–784.

[86] Chan, C. J., Whyte, G., Boyde, L., Salbreux, G., Guck, J., *Interface Focus* 2014, *4*, 1–11.

[87] Peterman, E. J. G., Gittes, F., Schmidt, C. F., *Biophys. J.* 2003, *84*, 1308–1316.

[88] Hoffman, B. D., Massiera, G., Van Citters, K. M., Crocker, J. C., *Proc. Natl. Acad. Sci. USA* 2006, *103*, 10259–10264.

[89] Wang, N., Butler, J. P., Ingber, D. E., *Science* 1993, *260*, 1124–1127.

[90] Neuman, K. C., Lionnet, T., Allemand, J. F., *Annu. Rev. Mater. Res.* 2007, *37*, 33–67.

[91] Pankhurst, Q., Jones, S., Dobson, J., *J. Phys. D: Appl. Phys.* 2016, *49*.

[92] Bausch, A. R., Ziemann, F., Boulbitch, A. A., Jacobson, K., Sackmann, E., *Biophys. J.* 1998, *75*, 2038–2049.

[93] McAndrew, C. P., Tyson, C., Zischkau, J., Mehl, P., Tuma, P. L., Pegg, I. L., Sarkar, A., *BioTechniques* 2016, *60*, 21–27.

[94] Haber, C., Wirtz, D., *Rev. Sci. Instrum.* 2000, *71*, 4561–4570.

[95] Amblard, F., Maggs, A. C., Yurke, B., Pargellis, A. N., Leibler, S., *Phys. Rev. Lett.* 1996, *77*, 4470–4473.

[96] Bausch, A. R., Moller, W., Sackmann, E., *Biophys. J.* 1999, *76*, 573–579.

[97] Strick, T. R., Croquette, V., Bensimon, D., *Nature* 2000, *404*, 901–904.

[98] Wilhelm, C., Gazeau, F., Bacri, J. C., *Phys. Rev. E: Stat. Nonlinear Soft Matter Phys*. 2003, *67*, 1–12.

[99] Fabry, B., Maksym, G. N., Hubmayr, R. D., Butler, J. P., Fredberg, J. J., *J. Magn. Magn. Mater.* 1999, *194*, 120–125.

[100] Jubery, T. Z., Srivastava, S. K., Dutta, P., *Electrophoresis* 2014, *35*, 691–713.

[101] Engelhardt, H., Gaub, H., Sackmann, E., *Nature* 1984, *307*, 378–380.

[102] Seifert, U., *Adv. Phys.* 1997, *46*, 13–137.

[103] Dimova, R., Bezlyepkina, N., Jordo, M. D., Knorr, R. L., Riske, K. A., Staykova, M., Vlahovska, P. M., Yamamoto, T., Yang, P., Lipowsky, R., *Soft Matter* 2009, *5*, 3201–3212.

[104] Dimova, R., Riske, K. A., in: Miklavčič, D. (Ed.), *Handbook of Electroporation*, Springer International Publishing, Cham 2017, pp. 235–252.

[105] Riske, K. A., Dimova, R., *Biophys. J.* 2005, *88*, 1143–1155.

[106] Riske, K. A., Dimova, R., *Biophys. J.* 2006, *91*, 1778–1786.

[107] Salipante, P. F., Vlahovska, P. M., *Soft Matter* 2014, *10*, 3386–3393.

[108] Knorr, R. L., Staykova, M., Gracia, R. S., Dimova, R., *Soft Matter* 2010, *6*, 1990–1996.

[109] Vlahovska, P. M., *Annu. Rev. Fluid Mech.* 2019, *51*, 305–330.

[110] Zimmermann, U., Friedrich, U., Mussauer, H., Gessner, P., Hamel, K., Sukhoruhov, V., *IEEE Trans. Plasma Sci.* 2000, *28*, 72–82.

[111] MacQueen, L. A., Buschmann, M. D., Wertheimer, M. R., *J. Micromech. Microeng*. 2010, *20*, 1–11.

[112] Freedman, K. J., Ahn, C. W., Kim, M. J., *ACS Nano* 2013, *7*, 5008–5016.

[113] Bandara, Y. N. D., Karawdeniya, B. I., Dwyer, J. R., *ACS Omega* 2019, *4*, 226–230.

[114] Merchant, C. A., Healy, K., Wanunu, M., Ray, V., Peterman, N., Bartel, J., Fischbein, M. D., Venta, K., Luo, Z., Johnson, A. T. C., Drndić, M., *Nano Lett*. 2010, *10*, 2915–2921.

[115] Saharia, J., Bandara, Y. N. D., Goyal, G., Lee, J. S., Karawdeniya, B. I., Kim, M. J., *ACS Nano* 2019, *13*, 4246–4254.

[116] Freedman, K. J., Haq, S. R., Edel, J. B., Jemth, P., Kim, M. J., *Sci. Rep.* 2013, *3*, 1638.

[117] Freedman, K. J., Jürgens, M., Prabhu, A., Ahn, C. W., Jemth, P., Edel, J. B., Kim, M. J., *Anal. Chem.* 2011, *83*, 5137–5144.

[118] Karawdeniya, B. I., Bandara, Y. N. D., Nichols, J. W., Chevalier, R. B., Dwyer, J. R., *Nat. Commun.* 2018, *9*, 3278.

[119] McMullen, A., De Haan, H. W., Tang, J. X., Stein, D., *Nat. Commun.* 2014, *5*, 4171.

[120] Lee, J. S., Saharia, J., Bandara, Y. N. D., Karawdeniya, B. I., Goyal, G., Darvish, A., Wang, Q., Kim, M. J., Kim, M. J., *Electrophoresis* 2019, *40*, 1337–1344.

[121] Goyal, G., Freedman, K. J., Kim, M. J., *Anal. Chem.* 2013, *85*, 8180–8187.

[122] Robertson, J. W., Rodrigues, C. G., Stanford, V. M., Rubinson, K. A., Krasilnikov, O. V., Kasianowicz, J. J., *Proc. Natl. Acad. Sci. USA* 2007, *104*, 8207–8211.

[123] Bandara, Y. N. D., Nichols, J. W., Karawdeniya, I. B., Dwyer, J. R., *Electrophoresis* 2018, *39*, 626–634.

[124] Karawdeniya, B. I., Bandara, Y. N. D., Nichols, J. W., Chevalier, R. B., Hagan, J. T., Dwyer, J. R., *J. Anal. Test.* 2019, *3*, 61–79.

[125] Grover, N., Naaman, J., Ben-Sasson, S., Doljanski, F., *Biophys. J.* 1969, *9*, 1398–1414.

[126] Dwyer, J. R., Bandara, Y. M. N. D. Y., Whelan, J. C., Karawdeniya, B. I., Nichols, J. W., in: Joshua Edel, A. I., Kim M. J. (Ed.), *Nanofluidics*, The Royal Society of Chemistry, London, UK 2017, pp. 190–236.

[127] Lee, J. S., Peng, B., Sabuncu, A. C., Nam, S., Ahn, C., Kim, M. J., Kim, M., *Electrophoresis* 2018, *39*, 833–843.

[128] Saville, D. A., *Annu. Rev. Fluid Mech.* 1997, *29*, 27–64.

[129] Melcher, J. R., Taylor, G. I., *Annu. Rev. Fluid Mech.* 1969, *1*, 111–146.

[130] Taylor, G. I., *Proc. R. Soc. London Ser. A* 1966, *291*, 159–166.

[131] Morshed, A., Dutta, P., Hossan, M. R., Dillon, R., *Phys. Rev. Fluids* 2018, *3*, 1–18.

[132] Chen, C. H., *Electrokinetics Electrohydrodynamics Microsyst*. 2011, *530*, 177–220.

[133] Hossan, M. R., Dillon, R., Roy, A. K., Dutta, P., *J. Colloid Interface Sci.* 2013, *394*, 619–629.

[134] Hossan, M. R., Dillon, R., Dutta, P., *J. Comput. Phys.* 2014, *270*, 640–659.

[135] Hossan, M. R., Dutta, D., Islam, N., Dutta, P., *Electrophoresis* 2018, *39*, 702–731.

[136] Seiwert, J., Miksis, M. J., Vlahovska, P. M., *J. Fluid Mech.* 2012, *706*, 58–70.

[137] Grosse, C., Schwan, H. P., *Biophys. J.* 1992, *63*, 1632–1642.

[138] Li, H., Yang, J., Chu, T. T., Naidu, R., Lu, L., Chandramohanadas, R., Dao, M., Karniadakis, G. E., *Biophys. J.* 2018, *114*, 2014–2023.

[139] Zuo, J., Chung, T.-S., *Water* 2016, *8*, 586.

[140] Fung, Y.-C., *Biomechanics: Mechanical Properties of Living Tissues*, Springer-Verlag, Berlin, Germany 1981.

[141] Barthès-Biesel, D., Diaz, A., Dhenin, E., *J. Fluid Mech.* 2002, *460*, 211–222.

[142] Green, A. E., Adkins, J. E., *Large Elastic Deformations*, Clarendon Press, Oxford, UK 1970.

[143] Evans, E. A., Skalak, R., *Mechanics and Thermodynamics of Biomembranes*, CRC Press, Boca Raton, FL 1980.

[144] Pozrikidis, C., *Modeling and Simulation of Capsules and Biological Cells*, Chapman & Hall/CRC, London, UK 2003, pp. 35–101.

[145] Canham, P. B., *J. Theor. Biol.* 1970, *26*, 61–81.

[146] Helfrich, W., *Z. Naturforsch. C* 1973, *28*, 693–703.

[147] Barthes-Biesel, D., *Annu. Rev. Fluid Mech.* 2016, *48*, 25–52.

[148] Schwalbe, J. T., Vlahovska, P. M., Miksis, M. J., *Phys. Rev. E: Stat. Nonlinear Soft Matter Phys*. 2011, *83*, 046309.

[149] Dimova, R., Riske, K. A., Aranda, S., Bezlyepkina, N., Knorr, R. L., Lipowsky, R., *Soft Matter* 2007, *3*, 817–827.

[150] Yamamoto, T., Aranda-Espinoza, S., Dimova, R., Lipowsky, R., *Langmuir* 2010, *26*, 12390–12407.

[151] Aranda, S., Riske, K. A., Lipowsky, R., Dimova, R., *Biophys. J.* 2008, *95*, L19–L21.

[152] Hyuga, H., Kinosita, K., Wakabayashi, N., *Jpn. J. Appl. Phys. Part 1* 1991, *30*, 1141–1148.

[153] Hyuga, H., Kinosita, K., Wakabayashi, N., *Jpn. J. Appl. Phys. Part 1* 1991, *30*, 1333–1335.

[154] Sadik, M. M., Li, J. B., Shan, J. W., Shreiber, D. I., Lin, H., *Physical Review E: Stat. Nonlinear Soft Matter Phys*. 2011, *83*, 066316.

[155] Kolahdouz, E. M., Salac, D., *SIAM J. Sci. Comp.* 2015, *37*, B473–B494.

[156] Veerapaneni, S., *J. Comput. Phys.* 2016, *326*, 278–289.

[157] Zhang, J., Zahn, J. D., Tan, W. C., Lin, H., *Phys. Fluids* 2013, *25*, 1–18.

[158] Yu, M., Lira, R. B., Riske, K. A., Dimova, R., Lin, H., *Phys. Rev. Lett.* 2015, *115*, 128303.

[159] Gracia, R. S., Bezlyepkina, N., Knorr, R. L., Lipowsky, R., Dimova, R., *Soft Matter* 2010, *6*, 1472–1482.

[160] Portet, T., Dimova, R., *Biophys. J.* 2010, *99*, 3264–3273.

[161] Salipante, P. F., Knorr, R. L., Dimova, R., Vlahovska, P. M., *Soft Matter* 2012, *8*, 3810–3816.

[162] Morshed, A., Dutta, P., Kim, M. J., *Electrophoresis* 2019, *40*, 2584–2591.

[163] Favre, M., Polesel-Maris, J., Overstolz, T., Niedermann, P., Dasen, S., Gruener, G., Ischer, R., Vettiger, P., Liley, M., Heinzelmann, H., Meister, A., *J. Mol. Recognit.* 2011, *24*, 446–452.

